2.2.2-Cryptand Complexes of Neptunium(III) and Plutonium(III)

Conrad A. P. Goodwin, †[a] Sierra R. Ciccone, †[b] Samuel Bekoe,[b] Sourav Majumdar,[b] Brian L. Scott,[c] Joseph W. Ziller,[b] Andrew J. Gaunt,*[a] Filipp Furche,*[b], and William J. Evans*[b]

[a] Chemistry Division, Los Alamos National Laboratory, Los Alamos, NM 87545 (USA)

[b] Department of Chemistry, University of California, Irvine, California 92697-2025, United States

[c] Materials Physics & Applications Division, Los Alamos National Laboratory, Los Alamos, NM 87545 (USA)

*To whom correspondence should be addressed. wevans@uci.edu; filipp.furche@uci.edu; gaunt@lanl.gov

†These authors contributed equally to this work.

Table of Contents

S1. Experimental Details

General considerations

Caution! *The ^{237}Np (t$_{½}$ = 2.144×10^6 years)[1] and ^{239}Pu (t$_{½}$ = 24,110 years)[1] isotopes – and their daughters – present serious health threats due to their* α-, β-, *and* γ-*emissions.* Hence, all studies that involved manipulation of these isotopes were conducted in a radiation laboratory equipped with high efficiency particulate air (HEPA) filtered hoods and in negative pressure gloveboxes. Additional safeguards included continuous air monitoring and use of hand-held radiation monitoring equipment. Entrance to the laboratory space was controlled with a hand and foot radiation monitoring instrumentation and a full body personal contamination monitoring station. The handling of free-flowing transuranium-containing solids was restricted to be within negative pressure gloveboxes equipped with HEPA filters. Due to these radiological hazards, elemental analyses were not possible for materials containing transuranium elements.

Unless otherwise described, all syntheses and manipulations were conducted under UHP argon (AirGas) or UHP helium (AirGas) with rigorous exclusion of oxygen and water using Schlenk line and glove box techniques (employing a negative-pressure, transuranium capable, helium atmosphere glovebox where required). 4 Å molecular sieves were activated by heating for 36 hours at 200 °C, 10^{-4} mbar. Anhydrous inhibitor-free THF (Sigma Aldrich), anhydrous C$_6$H$_6$ (Sigma Aldrich), and THF-d_8 (Sigma Aldrich) were transferred onto activated 4 Å molecular sieves, stored for 1 week and degassed before use. Anhydrous Et$_2$O (Sigma Aldrich, containing 1% BHT) was degassed, stirred with Na/Ph$_2$CO for several days until a persistent red/purple colour was observed, then distilled onto activated 4 Å molecular sieves. All solvents were tested with a dilute THF solution of Na$_2$Ph$_2$CO (150 mg Ph$_2$CO in 20 mL of THF with an excess of Na metal) such that ethers required 1 drop / mL to retain purple coloration and hydrocarbon solvents required 1 drop / 2 mL. [AnI$_3$(THF)$_4$] (An = Np, Pu) were prepared as described elsewhere.[2] 4,7,13,16,21,24-Hexaoxa-1,10-diazabicyclo[8.8.8]hexacosane, henceforth 2.2.2-crypt, was dried under dynamic vacuum (10^{-4} mbar) for 48 hours before use. The glovebox atmosphere was maintained with a standalone

Vacuum Atmosphere Genesis™ oxygen and moisture removal system, and atmosphere suitability was verified using a dilute toluene solution of $[Ti(Cp)_2(\mu-Cl)]_2$ (200 mg of commercial $[Ti(Cp)_2(Cl)_2]$ reduced over an excess of Zn powder in 20 mL of toluene, and filtered) prior to any manipulations, such that the residue dried to a dark green color each time (a color change to yellow or orange indicates decomposition of the Ti test compound and atmospheric O_2 removal is required). For transuranium work, all glassware, and glass-fiber filter discs, was stored in a vacuum oven (>150 °C) for 24 hours prior to being brought into the glovebox, and FEP (fluorinated ethylene propylene) NMR liners were brought into the box *via* overnight or multi-hour vacuum cycles. Transuranium crystals for single-crystal X-ray diffraction were mounted in Paratone-N or NVH oil inside 0.5 mm quartz capillaries (Charles Supper). The quartz capillaries were inserted through Parafilm plugs and placed inside test tubes to allow handling inside the transuranium glovebox while mounting crystals without contaminating the exterior surface of the capillary. The capillaries were then cut to appropriate size for later goniometer mounting with nail clippers. The ends of the cut capillaries were sealed with hot capillary wax before being removed from the glovebox for coating in clear nail varnish (Hard as Nails™) to provide shatter-resilience.[3] During the clipping and wax sealing steps, care must be taken to avoid the capillary touching any contaminated surfaces (this is achieved by the introduction of fresh petri dishes, forceps, clippers, and wax, as needed in conjunction with careful handling techniques to avoid contamination transfer). Solution phase electronic absorption spectra were collected at ambient temperature using a Varian Cary 6000i UV-vis-NIR spectrometer. The solution was contained in a low volume (1 mL) screw-capped quartz cuvette (1 cm path length) that was loaded in a transuranium glovebox (or HEPA filtered fume hood as appropriate) using Parafilm to protect the exterior surface of the cuvette and cap from radioactive contamination (parafilm removed in fume hood prior to data acquisition). Data was collected from 40,000 to 6,250 cm^{-1} (250 to 1,600 nm). For NMR spectroscopy, solution was loaded into a fresh FEP NMR liner that was protected from surface contamination with Parafilm while inside a transuranium glovebox. The liner was sealed with two PTFE plugs (the portion of the upper protruding plug was covered with masking tape), brought out of the glovebox and verified to be free of surface contamination before the parafilm/tape was removed and the liner loaded into a J. Young tap appended 5 mm NMR tube. The

headspace was then evacuated and refilled with He to provide an inert atmosphere above the sample. NMR data collection was performed on a Bruker Avance II at room temperature unless otherwise indicated. The spectra were referenced to internal solvent residuals (^{1}H and ^{13}C) or externally to 10% TMS in CDCl$_3$ (^{19}F) *via* Equation S1, which is the IUPAC recommended convention.

$$\Delta\ (Hz) = \frac{SR^{1H}}{SF^{1H}} \times SF^{NUC}$$

Equation S1. Where SR^{1H} is the spectrum reference frequency (in Hz) of a reference ^{1}H NMR spectrum collected with TMS set to 0 ppm collected under the same experimental conditions; SF^{1H} is the spectrometer frequency (in MHz) for the ^{1}H nucleus; SF^{NUC} is the spectrometer frequency (in MHz) of the nucleus in question. The answer is given in Hz, and is equal the amount the current peak is shifted by, for example a negative answer indicates the peak in question is shifted negatively by the magnitude of your answer; thus, the magnitude (in ppm) should be added to the current peak.

Where ε values are reported for molecular complexes below there is a modest error due to the small quantities of weighed material, as is nearly always the case when these values are reported from synthetic chemistry (as opposed analytical determination methods). Nonetheless it is a useful metric to determine based on weight of crystal dissolved and solvent weight.

*Synthesis of [An(2.2.2-crypt)(OTf)$_2$][OTf] (An = U, **1-U**; Np, **1-Np**; Pu, **1-Pu**)*

Synthesis of [U(2.2.2-crypt)(OTf)$_2$][OTf] (1-U). A suspension of [U(crypt)(I)$_2$][I] (100 mg, 100 µmol) in C$_6$H$_6$ (10 mL) was added to a stirring solution of Me$_3$SiOTf (300 µmol) in C$_6$H$_6$ (5 mL). During the course of addition, the solids dissolved quickly and then deposited a small quantity of green solids that appeared oily or greasy. The mixture was then left to stir overnight. The next day, the mixture was centrifuged to yield a green oily deposit and a colorless clear supernatant. The supernatant was decanted and the oil was taken up in THF, and the green solution was filtered and dried in vacuo to give a fluffy green solid (70 mg, 66% yield). The green solid was dissolved in THF, layered with Et$_2$O, and placed at −35 °C. Pale green plates of [U(2.2.2-crypt)(OTf)$_2$][OTf] (**1-U**) formed overnight, from which the structure was determined. ^{1}H NMR (THF-d_8, 400.13 MHz, 298 K): δ = 8.24. ^{19}F{^{1}H} NMR (THF-d_8, MHz, 298 K): δ = −80.32 (OTf, O$_3$SCF$_3$ × 3) UV-vis-NIR (THF): λ_{max} (cm^{-1}; ε) = 252 (39,680, 962), 271 (36,900, 890), 291 (34,360, 1,261), 310 (32,260, 1,337), 346 (28,900, 1,643), 374 (26,740, 1,472), 388 (25,770, 1,375), 412 (24,270, 1,198), 425 (23,530, 950), 444 (22,520, 490), 480 (20,830, 127), 515 (19,420, 146), 553 (18,080, 57), 570 (17,540, 90), 582 (17,180, 75), 603 (16,580, 78), 618 (16,180, 54), 627 (15,950, 53), 639 (15,650, 55), 704 (14,200, 51), 841 (11,890, 94), 856 (11,680, 93), 874 (11,440, 86), 895 (11,170, 64), 950 (10,530, 48), 979 (10,210, 50), 986 (10,140, 53), 1032 (971, 80). Anal. Calcd for US$_2$F$_6$O$_{12}$N$_2$C$_{20}$H$_{36}$SO$_3$CF$_3$: C, 23.16; H, 3.42; N, 2.64. Found: C, 23.81; H, 3.26; N, 2.24.

Synthesis of [Np(2.2.2-crypt)(OTf)$_2$][OTf] (1-Np). A solution of 2.2.2-crypt (6.3 mg, 16.7 µmol) in THF (1 mL) was added to a dark orange solution of [NpI$_3$(THF)$_4$] (15.2 mg, 16.8 µmol) in THF (3 mL) at room temperature. A pale yellow precipitate immediately formed and the orange colour of the supernatant discharged to yellow. The suspension was stirred for 3 hours then the supernatant was decanted. THF (1 mL) was added and the yellow suspension was stirred for 2 minutes then Et$_2$O (3 mL) was added. The mixture was stirred for 2 minutes then stored at −35 °C for 10 minutes before the supernatant was decanted. The wash procedure was repeated once and the resultant yellow powder was dried *in vacuo* for 1 hour. The pale yellow powder of putative composition [Np(2.2.2-crypt)(I)][I]$_2$ (14.1 mg, 86 % w.r.t. Np) was suspended in C$_6$H$_6$ (8 mL) and solids which

were adhered to the vial walls were loosened with a spatula. This pale yellow suspension was added to a solution of Me₃SiOTf (9.5 mg, 42.7 µmol) in C_6H_6 (5 mL). During the course of addition, the solids dissolved quickly and then deposited a small quantity of darker solids that appeared oily or greasy. The mixture was stirred overnight (14 hours). The solution appeared clear and pale yellow the next day with no solids present. THF (1 mL), Et₂O (1 mL), and pentane (5 mL) were added to the solution which caused rapid precipitation of a fine grey powder. *This mixture was found to afford near-quantitative precipitation of the product as a powder rather than greasy solids*. The suspension was stored at −35 °C for 1 hour, then the supernatant was decanted. THF (1 mL) was added and the yellow suspension was stirred for 2 minutes then Et₂O (3 mL) was added. The mixture was stirred for 2 minutes then stored at −35 °C for 10 minutes before the supernatant was decanted. The wash procedure was repeated once and the resultant yellow powder was dried *in vacuo* for 1 hour. THF (2.5 mL) was added to the pale blue powder, and the suspension was gently warmed (45 °C hotplate) until the material dissolved. The solution was filtered into a 4 mL glass vial through 2 half-discs of glass microfiber mounted in a glass pipette, and then layered with Et₂O (1.5 mL). Storage of this vial at −35 °C overnight afforded pale blue plates of [Np(2.2.2-crypt)(OTf)₂][OTf] (**1-Np**) from which the structure was determined. Decantation and storage of the supernatant for a second night afforded an additional crop of crystalline **1-Np** (14 mg, 93 % w.r.t. putative [Np(2.2.2-crypt)(I)][I]₂). ¹H NMR (THF-d_8, 400.13 MHz, 298 K): δ = 1.14 (s, 12 H, N(C$\underline{H}$₂CH₂)), 6.12 (s, 12 H, N(CH₂C$\underline{H}$₂)), 10.85 (s, 12 H, O(C$\underline{H}$₂)₂O). ¹⁹F{¹H} NMR (THF-d_8, 376.46 MHz, 298 K): δ = −88.22 (OTf, O₃SCF₃ × 3. No additional resonances were observed at +300 to −500 ppm. UV-vis-NIR (THF): λ$_{max}$ (cm⁻¹; ε) = 256 (39,110, 1,390), 259 (38,570, 1,320), 263 (38,075, 892), 266 (37,530, 505), 283 (35,345, 25), 286 (34,990, 18), 288 (34,675, 15), 300 (33,315, 9), 302 (33,135, 9), 306 (32,705, 18), 308 (32,470, 28), 319 (31,380, 21), 321 (31,180, 18), 327 (30,600, 9), 330 (30,335, 13), 331 (30,170, 17), 333 (30,005, 18), 334 (29,920, 19), 357 (28,025, 11), 362 (27,635, 15), 367 (27,260, 15), 381 (26,270, 22), 390 (25,670, 24), 400 (25,005, 8), 417 (23,965, 13), 435 (23,010, 9), 439 (22,760, 9), 451 (22,150, 29), 456 (21,950, 22), 471 (21,220, 18), 701 (14,265, 14), 729 (13,710, 21), 749 (13,355, 34), 769 (13,010, 50), 873 (11,460, 10), 910 (10,990, 7).

Synthesis of [Pu(2.2.2-crypt)(OTf)$_2$][OTf] (1-Pu). The procedure above for **1-Np** was repeated using [PuI$_3$(THF)$_4$] (25 mg, 27.5 µmol) and 2.2.2-crypt (10.4 mg, 27.6 µmol). Cream-coloured putative [Pu(2.2.2-crypt)(I)][I]$_2$ (24.4 mg, 90% w.r.t. Pu) was treated with Me$_3$SiOTf (18.6 mg, 83.7 µmol). Two crystalline crops (3.7 mg, 14 % w.r.t. putative [Pu(2.2.2-crypt)(I)][I]$_2$) of pale lilac plates of [Pu(2.2.2-crypt)(OTf)$_2$][OTf] (**1-Pu**) were grown from THF (2 mL) layered with Et$_2$O (1 mL) stored at −35 °C, as above for **1-Np**. ^{1}H NMR (THF-d_8, 400.13 MHz, 298 K): δ = 3.25 (s, 12 H, N(C$\underline{H}_2$CH$_2$)), 4.05 (s, 12 H, N(CH$_2$C$\underline{H}_2$)), 4.29 (s, 12 H, O(C$\underline{H}_2$)$_2$O). ^{19}F{^{1}H} NMR (THF-d_8, 376.46 MHz, 298 K): δ = −79.77 (OTf, O$_3$SCF$_3$ × 3. No additional resonances were observed at +300 to −500 ppm. UV-vis-NIR (THF): λ$_{max}$ (cm^{-1}; ε) = 257 (38,915, 364), 269 (37,200, 32), 279 (35,800, 21), 297 (33,685, 11), 309 (32,330, 25), 313 (31,980, 25), 319 (31,310, 24), 321 (31,105, 18), 336 (29,735, 12), 371 (26,970, 14), 388 (25,755, 12), 416 (24,045, 11), 432 (23,160, 13), 480 (20,855, 15), 533 (18,770, 11), 555 (18,030, 10), 572 (17,470, 8), 863 (11,590, 7), 1,412 (7,080, 7).

The significant difference in yield is not due to any significant differences in solubility for **1-Pu** *versus* **1-Np**, but rather that the crystallization process is extremely sensitive to the ratio of Et$_2$O to THF. Crystallization that occurs too quickly affords spherical crystalline agglomerations, which are difficult to fully redissolve. Much of the yield loss occurred due to the repeated attempts at growing high-quality single-crystals for structure determination.
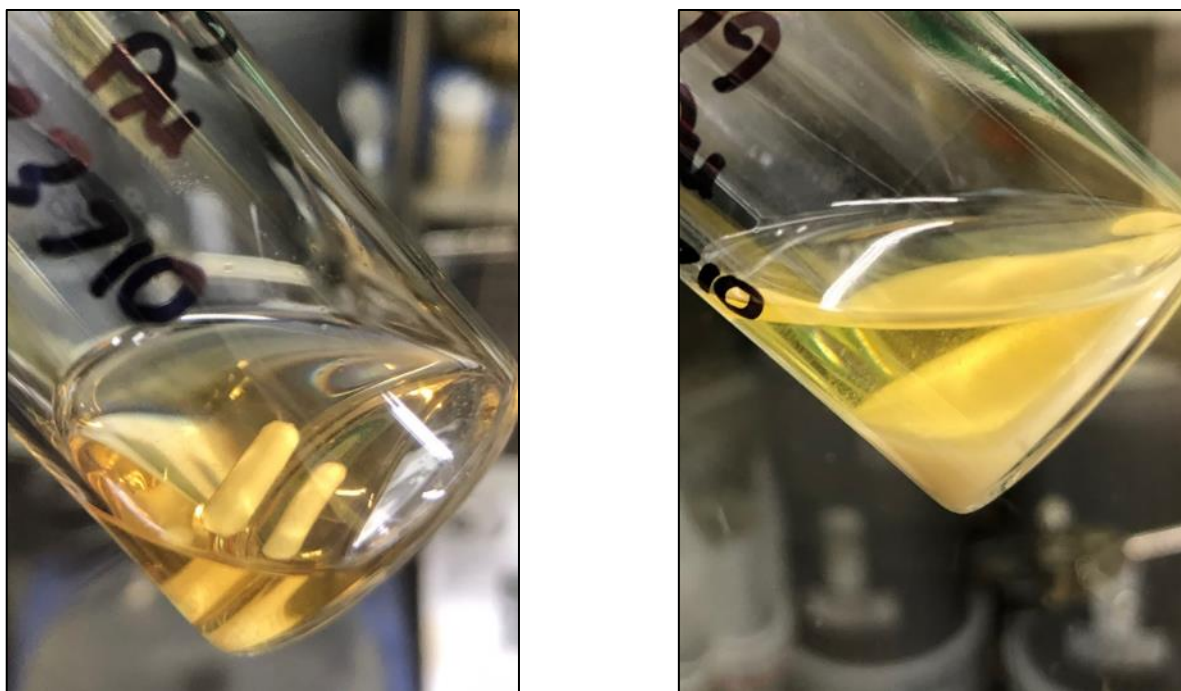
S2. Photographs taken during synthesis

Figure S1. From left to right: 1) A solution of [PuI$_3$(THF)$_4$] (**2-Pu**) in THF; 2) The same solution several minutes after treatment with 1 equivalent of 2.2.2-crypt with stirring, followed by settling.
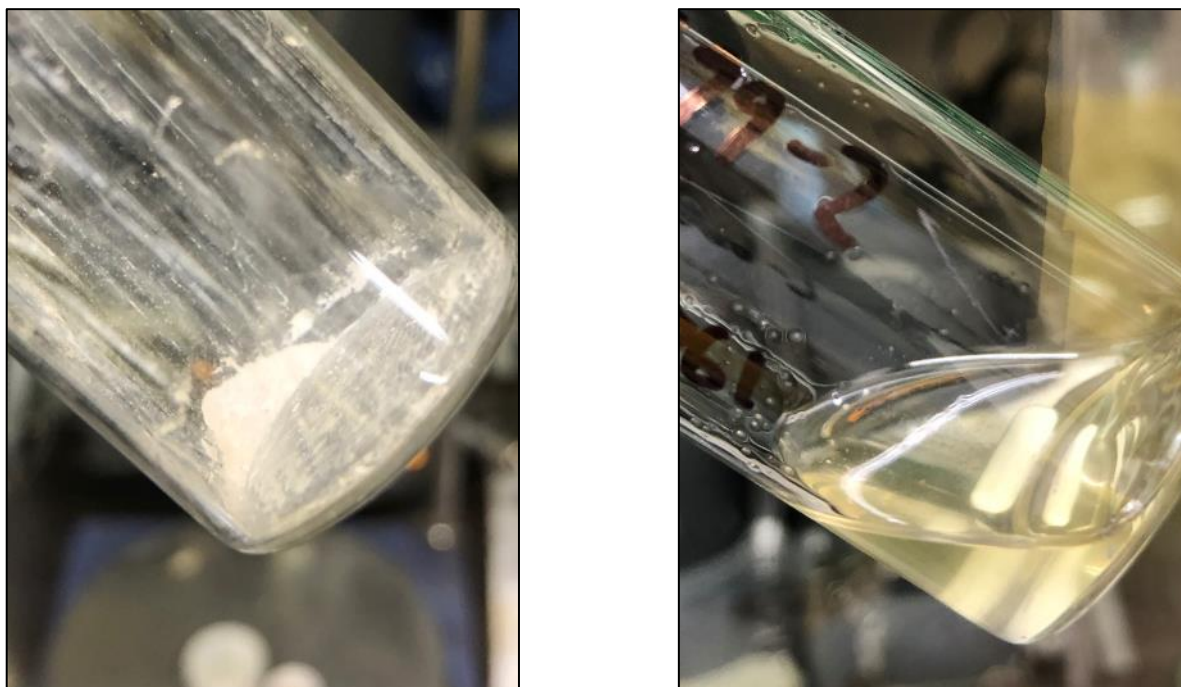

Figure S2. From left to right: 1) Putative [Pu(2.2.2-crypt)(I)][I]$_2$ after decanting the supernatant and washing with THF/Et$_2$O mixture; 2) The solution of Me$_3$SiOTf in C$_6$H$_6$ after addition of putative [Pu(2.2.2-crypt)(I)][I]$_2$ suspended in C$_6$H$_6$. The solid rapidly dissolved to leave a slightly turbid mixture.

Figure S3. The same reaction mixture as in Figure S2-R, after several minutes stirring. The pale lilac solids dissolved after stirring the mixture overnight.
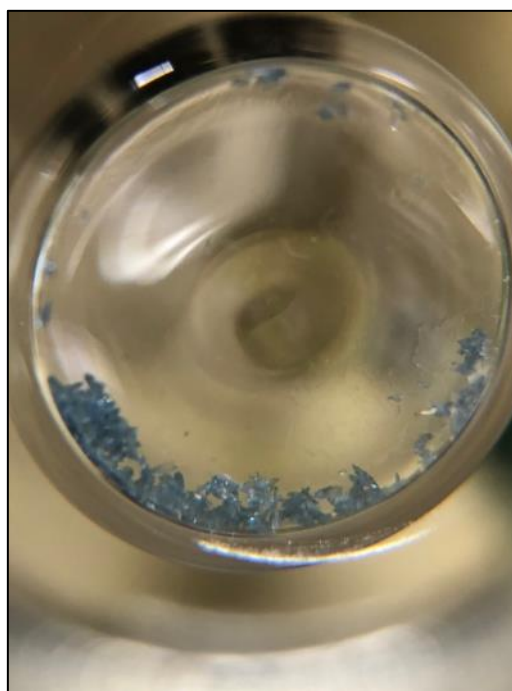
Figure S4. From left to right: 1) Crystals of [Np(2.2.2-crypt)(OTf)$_2$][OTf] (**1-Np**) that crystallized from THF (2.5 mL) layered with Et$_2$O (1 mL) at –35 °C; 2) The same crystals after isolation, and being washed with Et$_2$O (2 × 2 mL) and drying *in vacuo*.

Figure S5. From left to right1) Crystals of [Pu(2.2.2-crypt)(OTf)$_2$][OTf] (**1-Pu**) that crystallized from THF (2 mL) layered with Et$_2$O (1 mL) at –35 °C; 2) The same crystals after isolation, and being washed with Et$_2$O (2 × 2 mL) and drying *in vacuo*.

S3. Crystallography

General considerations

The crystal data for complexes **1-U**, **1-Np**, and **1-Pu** are compiled in Table S1. For **1-U**, a green crystal of approximate dimensions 0.152 x 0.197 x 0.265 mm was mounted in a cryoloop and transferred to a Bruker SMART APEX II diffractometer system. The APEX2[4] program package was used to determine the unit-cell parameters and for data collection (30 sec/frame scan time). The raw frame data was processed using SAINT[5] and SADABS[6] to yield the reflection data file. Subsequent calculations were carried out using the SHELXTL[7] program package. There were no systematic absences nor any diffraction symmetry other than the Friedel condition. The centrosymmetric triclinic space group $\bar{P}1$ was assigned and later determined to be correct.

The structure was solved by direct methods and refined on F^2 by full-matrix least-squares techniques. The analytical scattering factors[8] for neutral atoms were used throughout the analysis. Hydrogen atoms were included using a riding model. There were three molecules of the formula-unit present (Z = 6). Several atoms were disordered and included using multiple components with partial site-occupancy-factors. It was necessary to impose geometric restraints (DFIX)[7] and displacement constraints (EADP)[7] for fluorine atoms F(25), F(26) and F(27).

For **1-Np** and **1-Pu**, crystals were examined with a Bruker D8 Quest diffractometer equipped with a CMOS detector and microsource (Incoatec IµS 3.0) Mo Kα radiation (λ = 0.71073 Å). APEX III software was used for control and solving the unit cells prior to data collection. Intensities were integrated from data recorded on 0.5° (**1-Np**) by ω rotation with 1s (**1-Np**), or 3s (**1-Pu**) frame exposures. CrysAlisPro[9] was used for final unit cell determination and parameters were refined from the observed positions of all strong reflections in each data set. An analytical absorption correction was applied.[9] The Olex2[10] GUI was used for structure solution and refinement utilizing the ShelX software packages.[11] The structures were solved using ShelXT[11a]; the datasets were refined by ShelXL[11b] using full-matrix least-squares on all unique F^2 values, with anisotropic displacement parameters for all non-hydrogen atoms, and with constrained riding hydrogen geometries; U_{iso}(H) was set at 1.2 (1.5 for methyl groups if applicable) times Ueq of the parent atom. The largest features

in final difference syntheses were close to heavy atoms and were of no chemical significance. Olex2 combined with Inkscape was employed for molecular graphics.[10, 12] CCDC 2109157-2109159 contain the supplementary crystal data for this article. 2109157 (**1-U**) 2109158 (**1-Np**), and 2109159 (**1-Pu**). These data can be obtained free of charge from the Cambridge Crystallographic Data Centre via www.ccdc.cam.ac.uk/data_request/cif.

Table S1. Crystallographic data for **1-U**, **1-Np**, and **1-Pu**.

	1-U	1-Np	1-Pu
Internal identifier	src23	ms0602	ms0608
CCDC ref code	2109157	2109158	2109159
Formula	$US_2F_6O_{12}N_2C_{20}H_{36}SO_3CF_3$	$NpS_2F_6O_{12}N_2C_{20}H_{36}SO_3CF_3$	$PuS_2F_6O_{12}N_2C_{20}H_{36}SO_3CF_3$
Fw	1061.73	1060.70	1062.76
Crystal syst	Triclinic	Triclinic	Triclinic
Space group	$\bar{P}1$	$\bar{P}1$	$\bar{P}1$
a, Å	17.8696(18)	18.1717(6)	18.231(3)
b, Å	19.2980(19)	19.5134(6)	19.555(3)
c, Å	19.609(2)	19.6504(6)	19.607(3)
α, °	64.1427(14)	63.878(3)	64.334(16)
β, °	64.8810(14)	64.737(3)	64.496(16)
γ, °	62.8442(14)	62.556(3)	62.224(17)
V, Å^3	5195.3(9)	5328.5(3)	5340.2(18)
Z	6	6	6
ρ_{calcd}, g cm^{-3}	2.036	1.983	1.988
μ, mm^{-1}	4.983	3.215	2.140
$F(000)$	3102	3108	3114
Cryst size, mm	0.265 x 0.197 x 0.152	0.01 × 0.01 × 0.20	0.01 × 0.01 × 0.20
Temperature, K	133	100	100
no. reflections (unique)	77586 (28023)	49245 (20128)	43582 (20091)
R_{int}	0.0294	0.085	0.083
$R_1(wR_2)$ (F^2 > 2σ(F^2))[a]	0.0577 (0.1194)	0.0671 (0.1888)	0.0657 (0.1960)
S[a]	1.039	1.04	1.02
min./max. diff map, Å^{-3}	−1.978, 4.569	−1.34, 2.05	−1.72, 2.32

[a] $R = \sum ||F_O| - |F_C||/\sum |F_O|$; $R_W = [\sum w(F_O{}^2 - F_C{}^2)^2/\sum w(F_O{}^2)^2]^{0.5}$; $S = [\sum w(F_O{}^2 - F_C{}^2)^2/(\text{no. data} - \text{no. params})]^{0.5}$ for all data.

$$esd3 = \sqrt{(esd1)^2 + (esd2)^2}$$

Equation S2. The combined error from two individual metrics that have their own associated errors can be calculated as the root of the sum of the square of each error. This is not strictly appropriate for combining more than two individual errors.[13]

S4. UV-vis-NIR spectra

UV-vis-NIR spectra of [NpI₃(THF)₄]

[NpI₃(THF)₄]
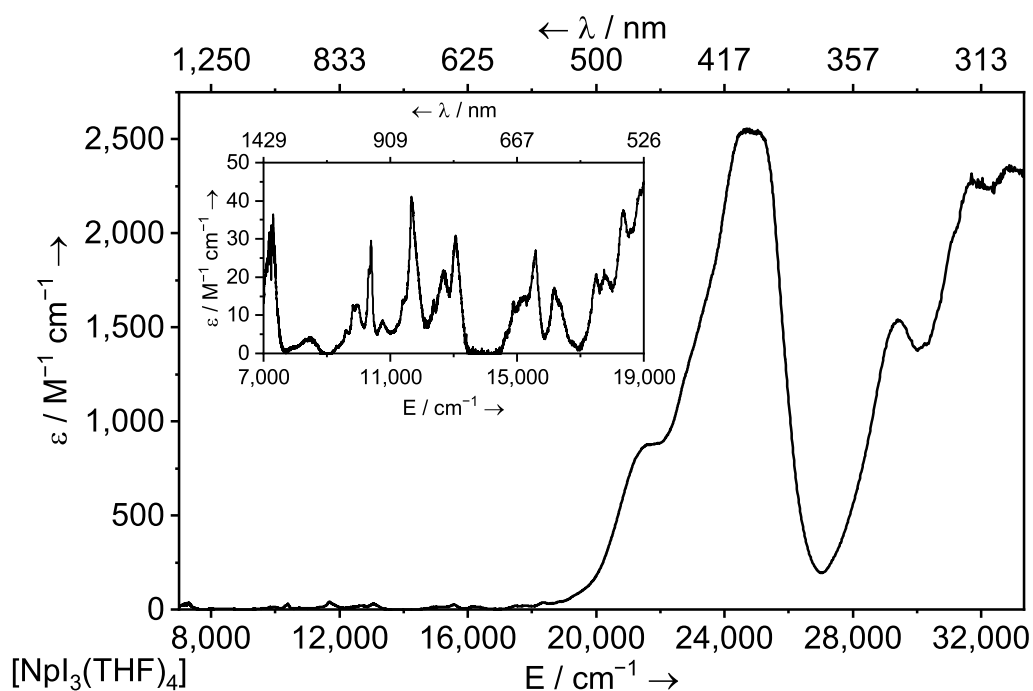
Figure S6. Solution UV-vis-NIR spectrum of [NpI3(THF)4] (1.05 mM) in THF shown between 7,000–33,333 cm⁻¹ (1,429–333 nm) at ambient temperature.

UV-vis-NIR spectra of [PuI₃(THF)₄]
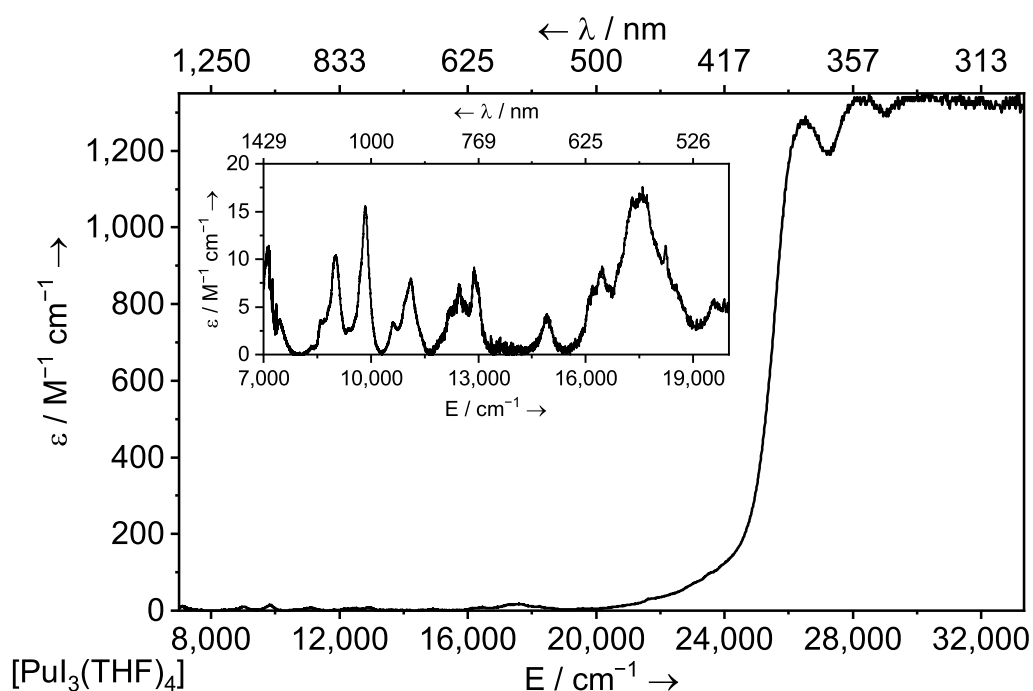
[PuI₃(THF)₄]

Figure S7. Solution UV-vis-NIR spectrum of [PuI3(THF)4] (1.98 mM) in THF shown between 7,000–33,333 cm⁻¹ (1,429–333 nm) at ambient temperature.

*UV-vis-NIR spectra comparing **1-An** and [AnI₃(THF)₄] (An = Np, Pu)*
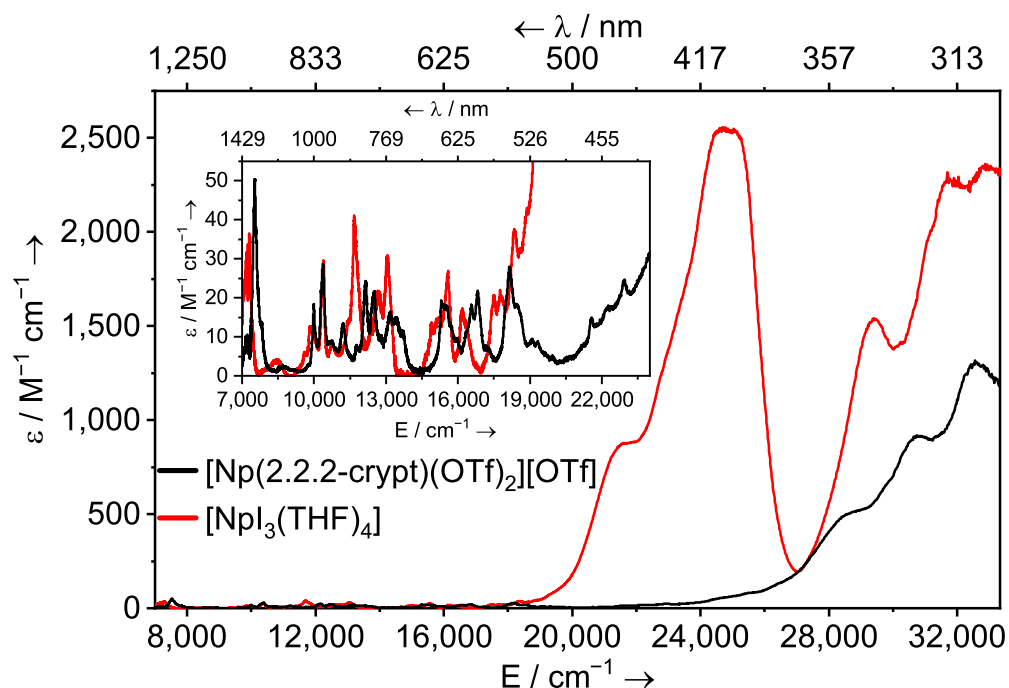
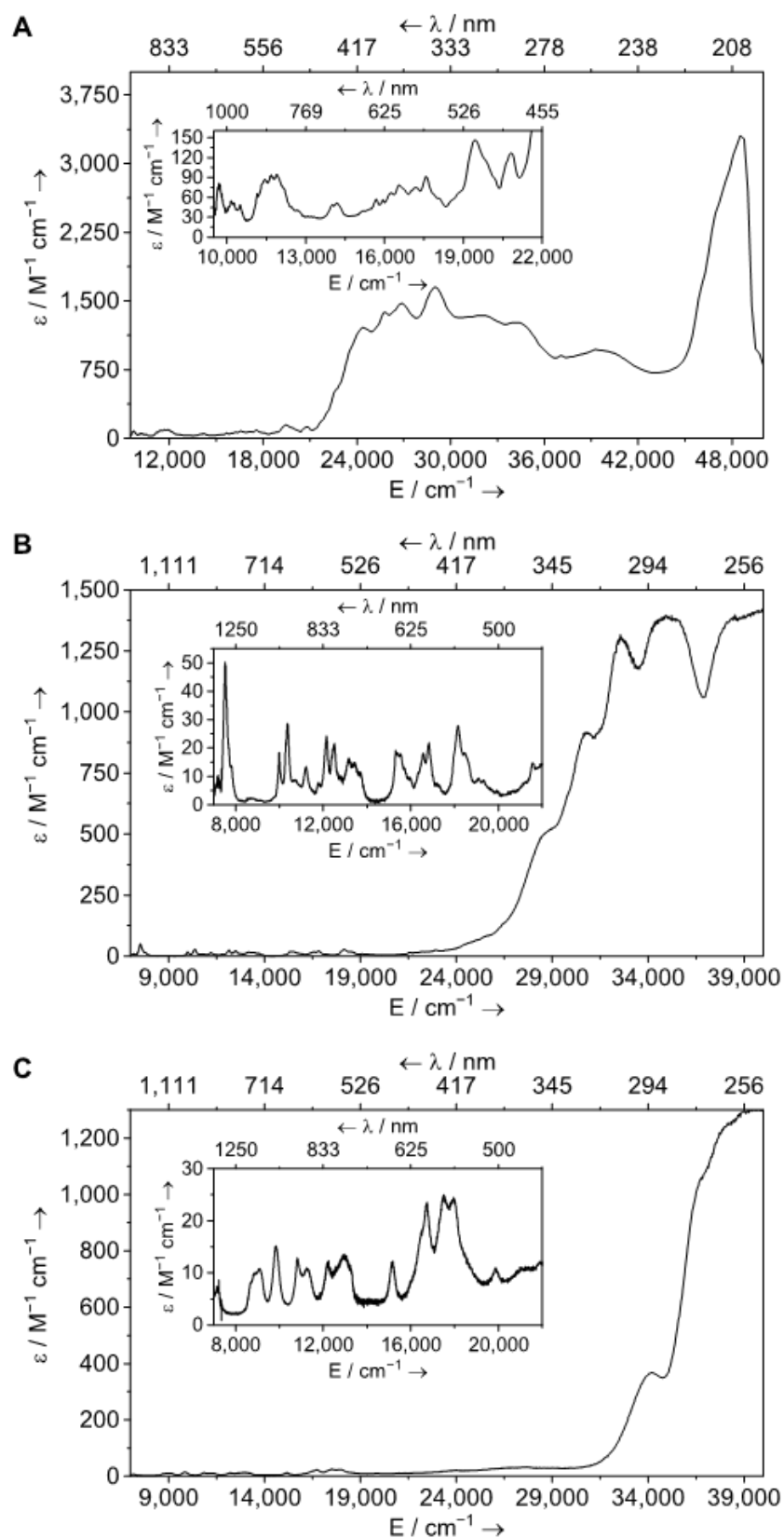
Figure S8. Solution UV-vis-NIR spectrum of [Np(2.2.2-crypt)(OTf)₂][OTf] (**1-Np**) (1.89 mM, THF, black line) and [NpI₃(THF)₄] (1.05 mM, THF, red line) shown between 7,000–33,333 cm⁻¹ (1,429–333 nm) at ambient temperature.
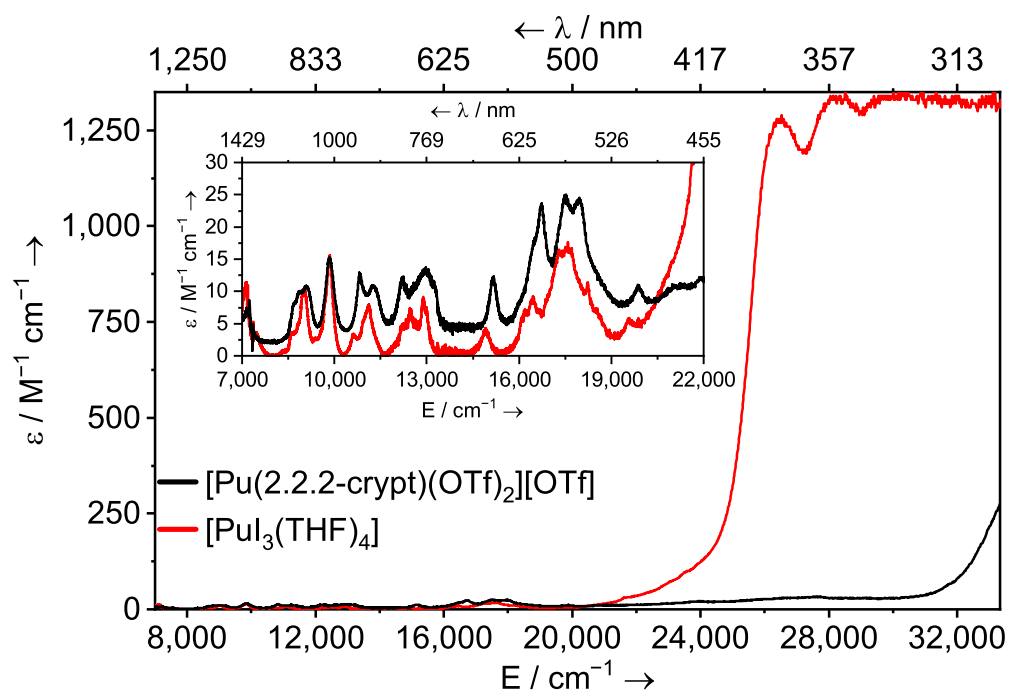
Figure S9. Solution UV-vis-NIR spectrum of [Pu(2.2.2-crypt)(OTf)₂][OTf] (**1-Pu**) (2.05 mM, THF, black line) and [PuI₃(THF)₄] (1.98 mM, THF, red line) shown between 7,000–33,333 cm⁻¹ (1,429–333 nm) at ambient temperature.

*UV-vis-NIR spectra comparing all **1-An** (An = U, Np, Pu)*

Figure S10. Solution UV-Vis-NIR spectrum of [U(crypt)(OTf)$_2$][OTf] (**1-U**) (5 mM) (**A**) shown between 9,500–50,000 cm^{-1}, and **1-Np** (1.89 mM) (**B**) and **1-Pu** (2.05 mM) (**C**) in THF shown between 7,000–33,333 cm^{-1} (1429–333 nm) at ambient temperature.
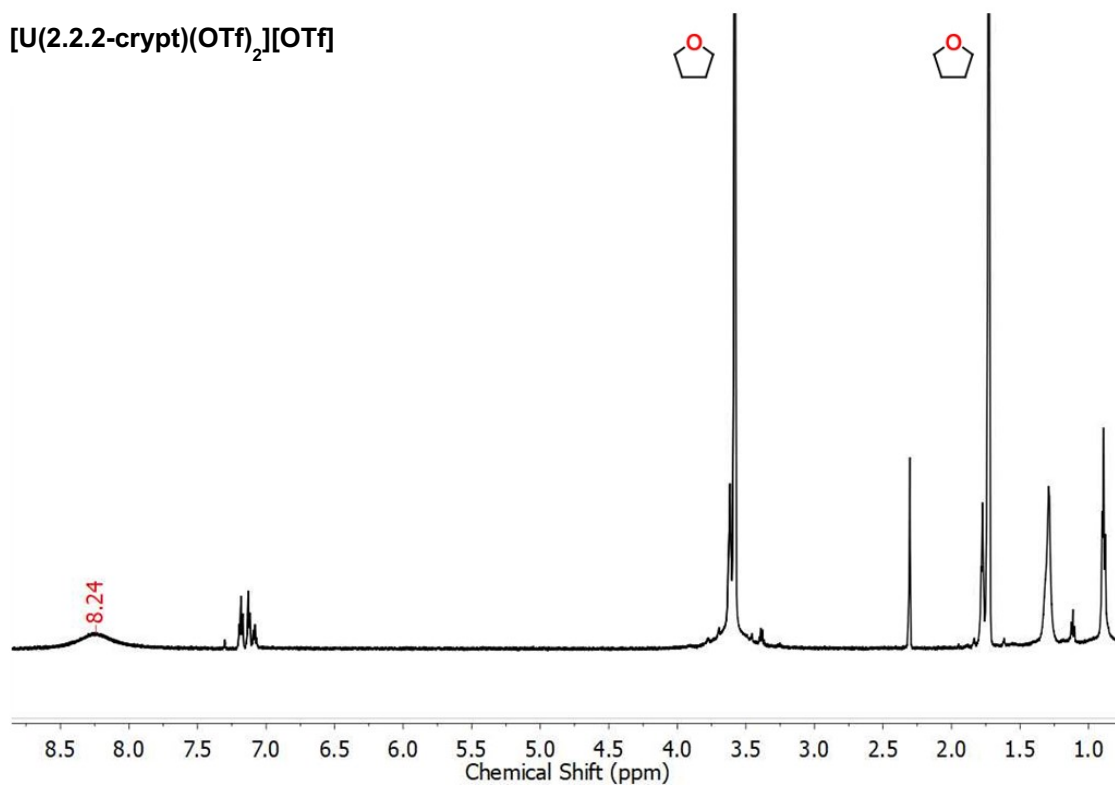
S5. NMR spectroscopy plots

[U(2.2.2-crypt)(OTf)$_2$][OTf]

Figure S11. ^{1}H NMR spectrum of [U(2.2.2-crypt)(OTf)$_2$][OTf] (**1-U**) in THF-d_8 collected at 298 K. No other peaks with significant intensity were observed between ±150 ppm. The NMR solvent residual is denoted. Only one resonance (at 8.24 ppm) is assigned to the complex. All other peaks are assigned to solvent.
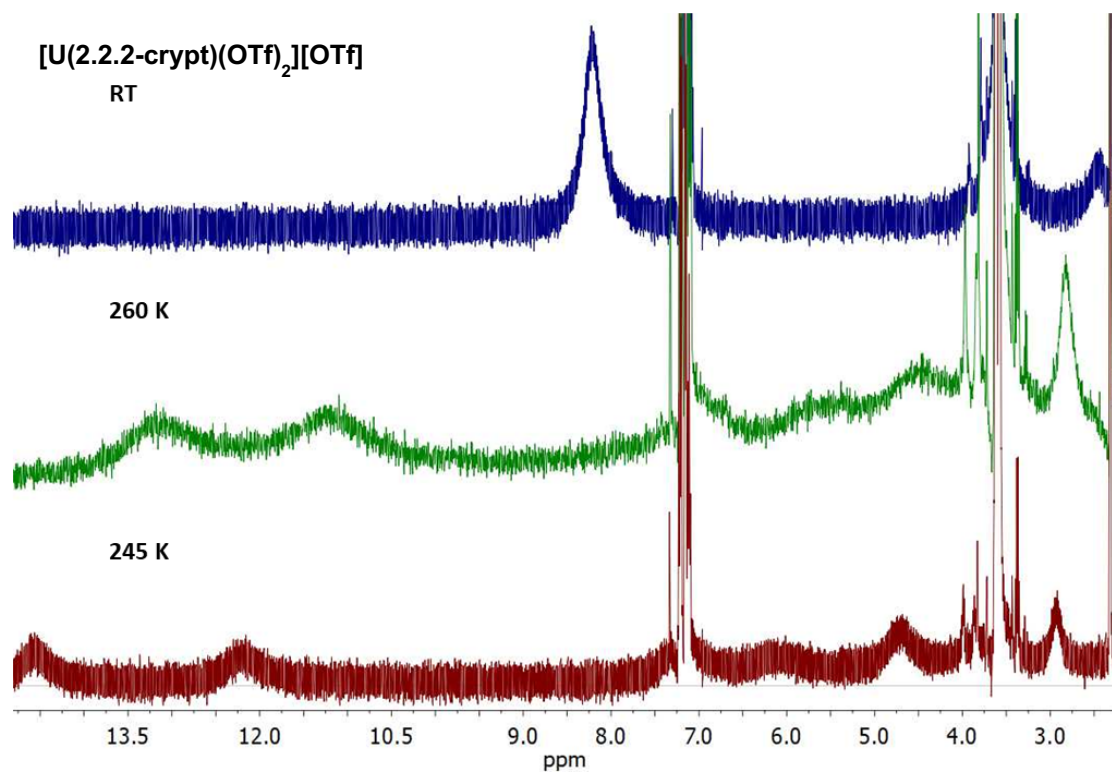
Figure S12. ^{1}H NMR spectrum of [U(2.2.2-crypt)(OTf)$_2$][OTf] (**1-U**) in THF-d_8 collected at variable temperatures. The broad resonance of **1-U** at 8.24 ppm at RT splits into several broad resonances at 260 K and at 245K. Even at 245K, a clearly resolved three-line spectrum was not able to be obtained.

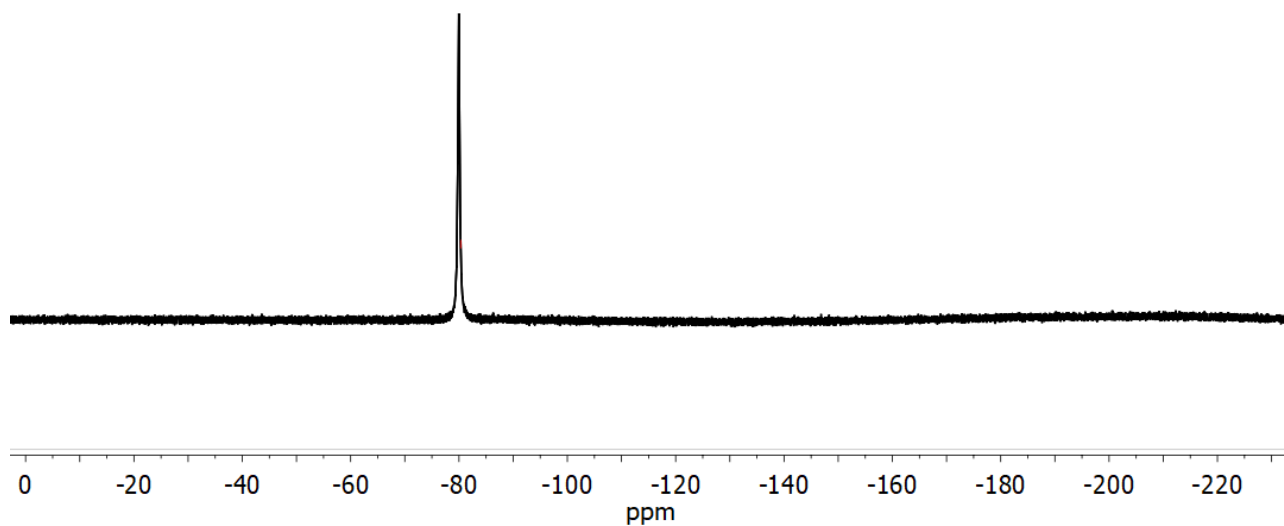[U(2.2.2-crypt)(OTf)$_2$][OTf]

−80.32

Figure S13. $^{19}F\{^1H\}$ NMR spectrum of [U(2.2.2-crypt)(OTf)$_2$][OTf] (**1-U**) in THF-d_8 collected at 298 K. No other peaks with significant intensity were observed between ±150 ppm. The presence of a single peak suggests that the bound and outer-sphere OTf ligands are in equilibrium at room temperature.

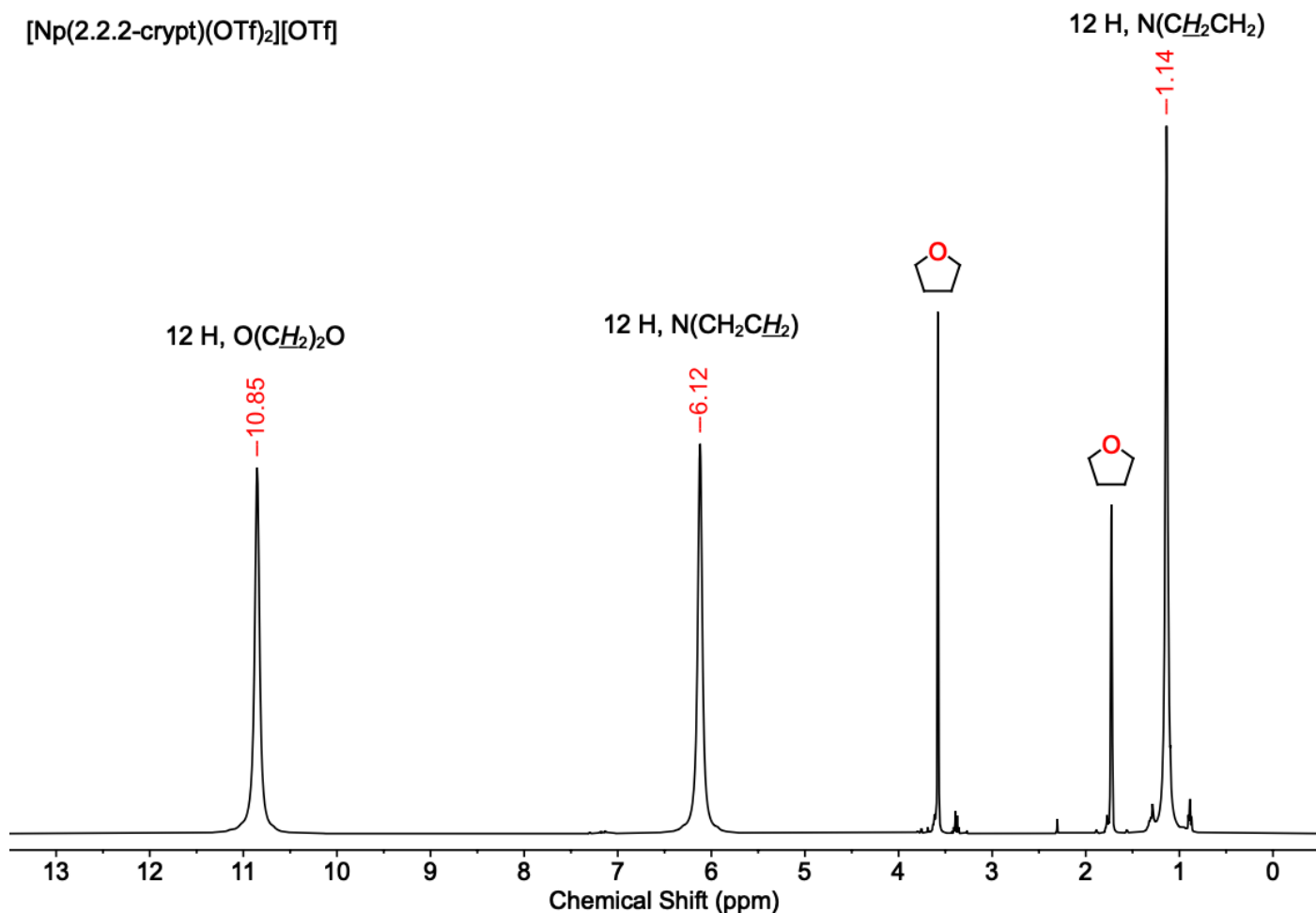**Figure S14.** ^{1}H NMR spectrum of [Np(2.2.2-crypt)(OTf)$_2$][OTf] (**1-Np**) in THF-d_8 collected at 298 K. No other peaks with significant intensity were observed between ±150 ppm. The NMR solvent residual is denoted. The peak at 1.14 ppm integrates to slightly more than 12 H as it overlaps with alkane impurities that derive from the NMR solvent and/or glovebox atmosphere.
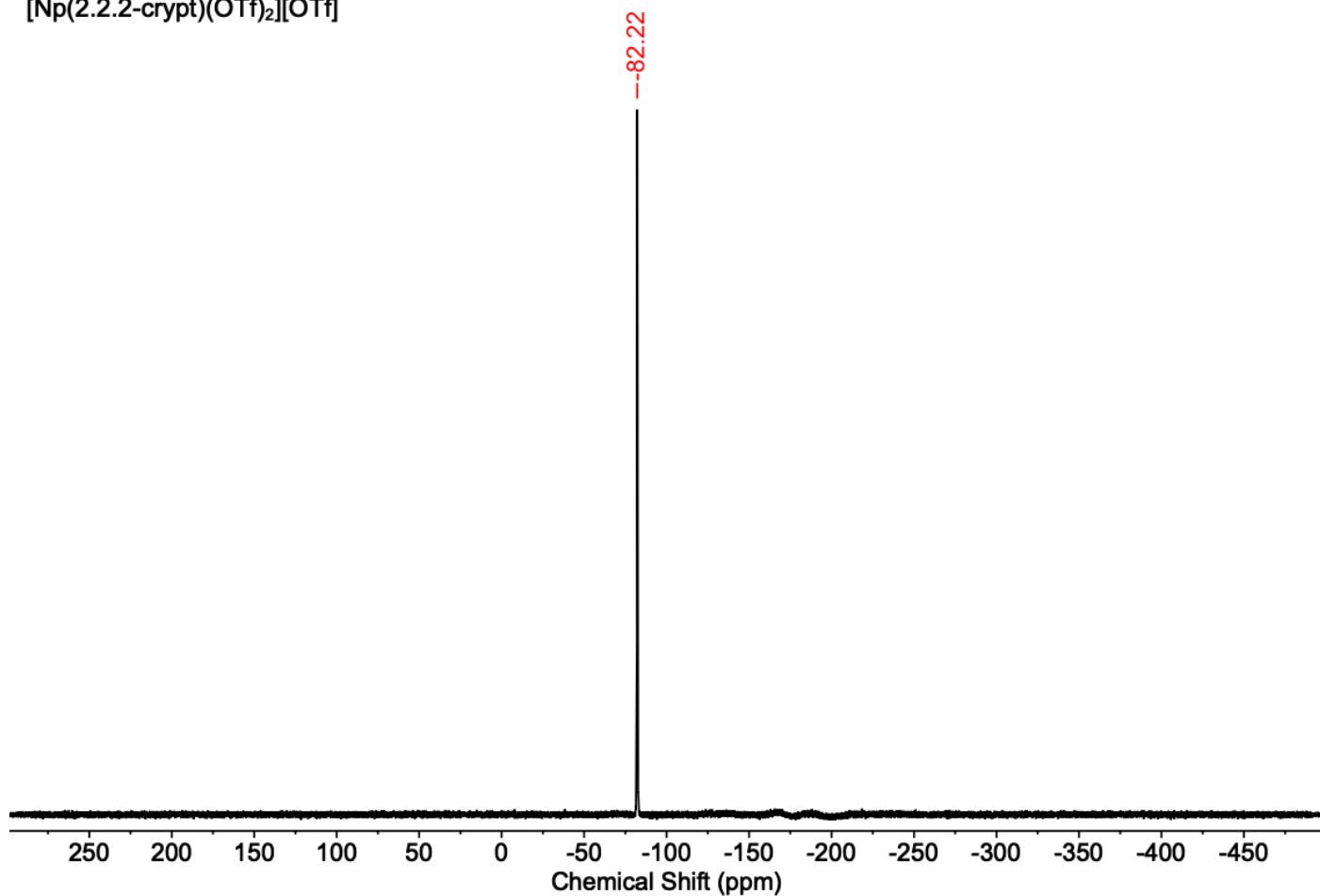
[Np(2.2.2-crypt)(OTf)₂][OTf]

−82.22

Figure S15. ^{19}F NMR spectrum of [Np(2.2.2-crypt)(OTf)$_2$][OTf] (**1-Np**) in THF-d_8 collected at 298 K. No other peaks with significant intensity were observed between ±150 ppm. The presence of a single peak suggests that the bound and outer-sphere OTf ligands are in equilibrium at room temperature. The artefacts between –225 and –150 are due to the FEP NMR tube liner that are part of our radiological control protocol. See below (Figure S20 and Figure S21) for spectra of a blank FEP tube.
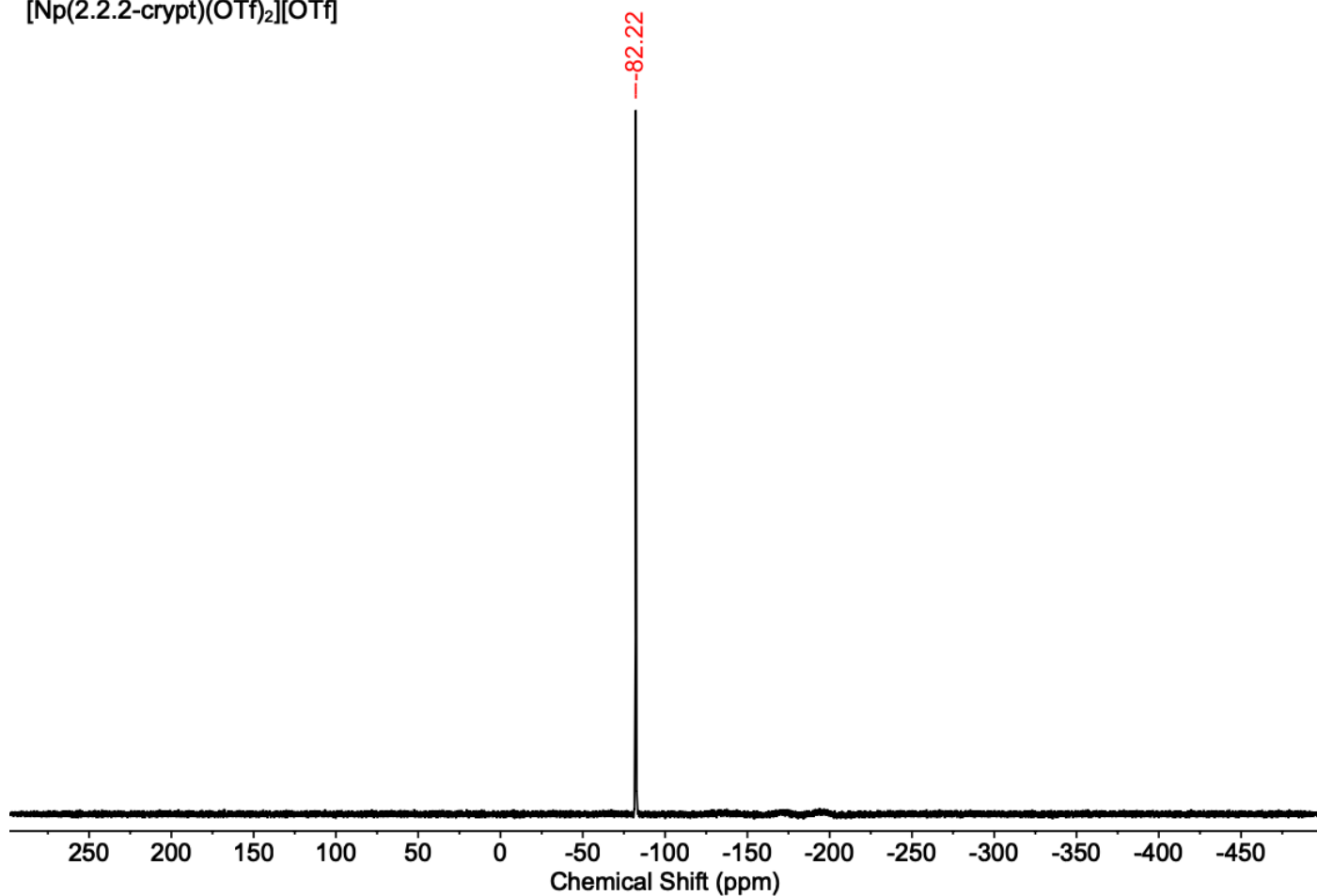
[Np(2.2.2-crypt)(OTf)₂][OTf]

−−82.22

Figure S16. $^{19}F\{^1H\}$ NMR spectrum of [Np(2.2.2-crypt)(OTf)₂][OTf] (**1-Np**) in THF-d_8 collected at 298 K. No other peaks with significant intensity were observed between ±150 ppm. The presence of a single peak suggests that the bound and outer-sphere OTf ligands are in equilibrium at room temperature. The artefacts between –225 and –150 are due to the FEP NMR tube liner that are part of our radiological control protocol. See below (Figure S20 and Figure S21) for spectra of a blank FEP tube.
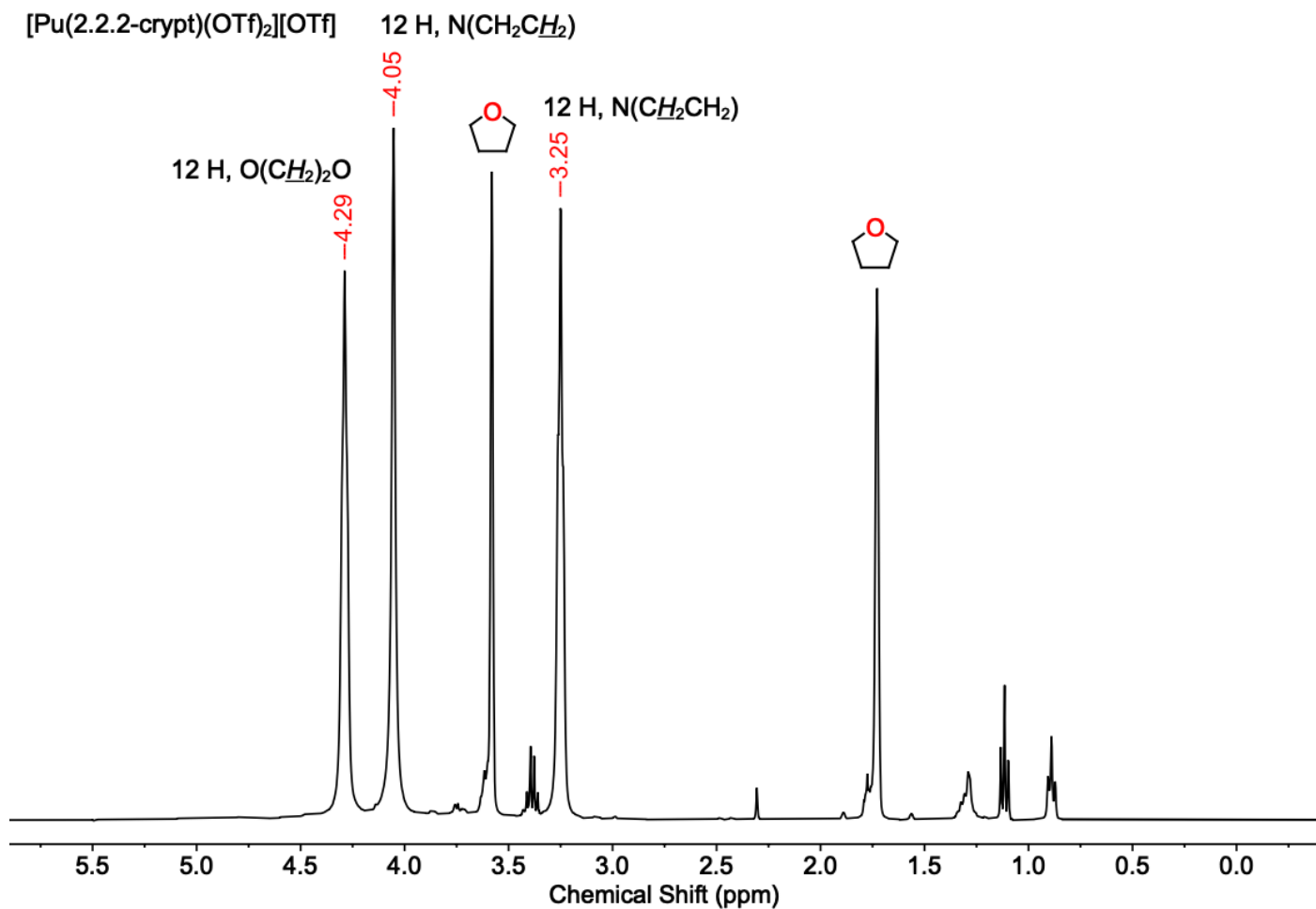
Figure S17. ^{1}H NMR spectrum of [Pu(2.2.2-crypt)(OTf)$_2$][OTf] (**1-Pu**) in THF-d_8 collected at 298 K. No other peaks with significant intensity were observed between ±150 ppm. The NMR solvent residual is denoted.

Figure S18. ^{19}F NMR spectrum of [Pu(2.2.2-crypt)(OTf)$_2$][OTf] (**1-Pu**) in THF-d_8 collected at 298 K. No other peaks with significant intensity were observed between ±150 ppm. The presence of a single peak suggests that the bound and outer-sphere OTf ligands are in equilibrium at room temperature. The artefacts between –225 and –150 are due to the FEP NMR tube liner that are part of our radiological control protocol. See below (Figure S20 and Figure S21) for spectra of a blank FEP tube.
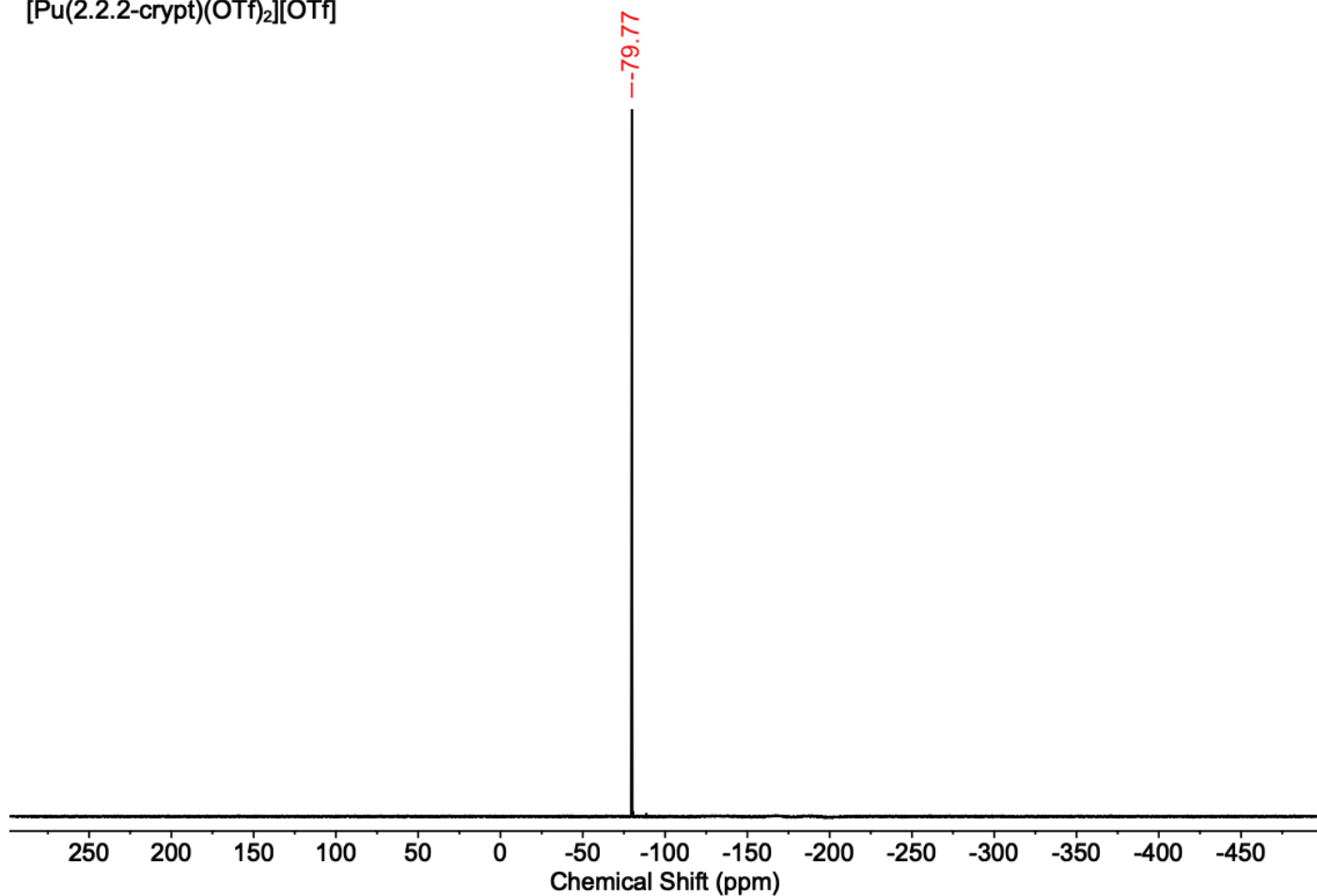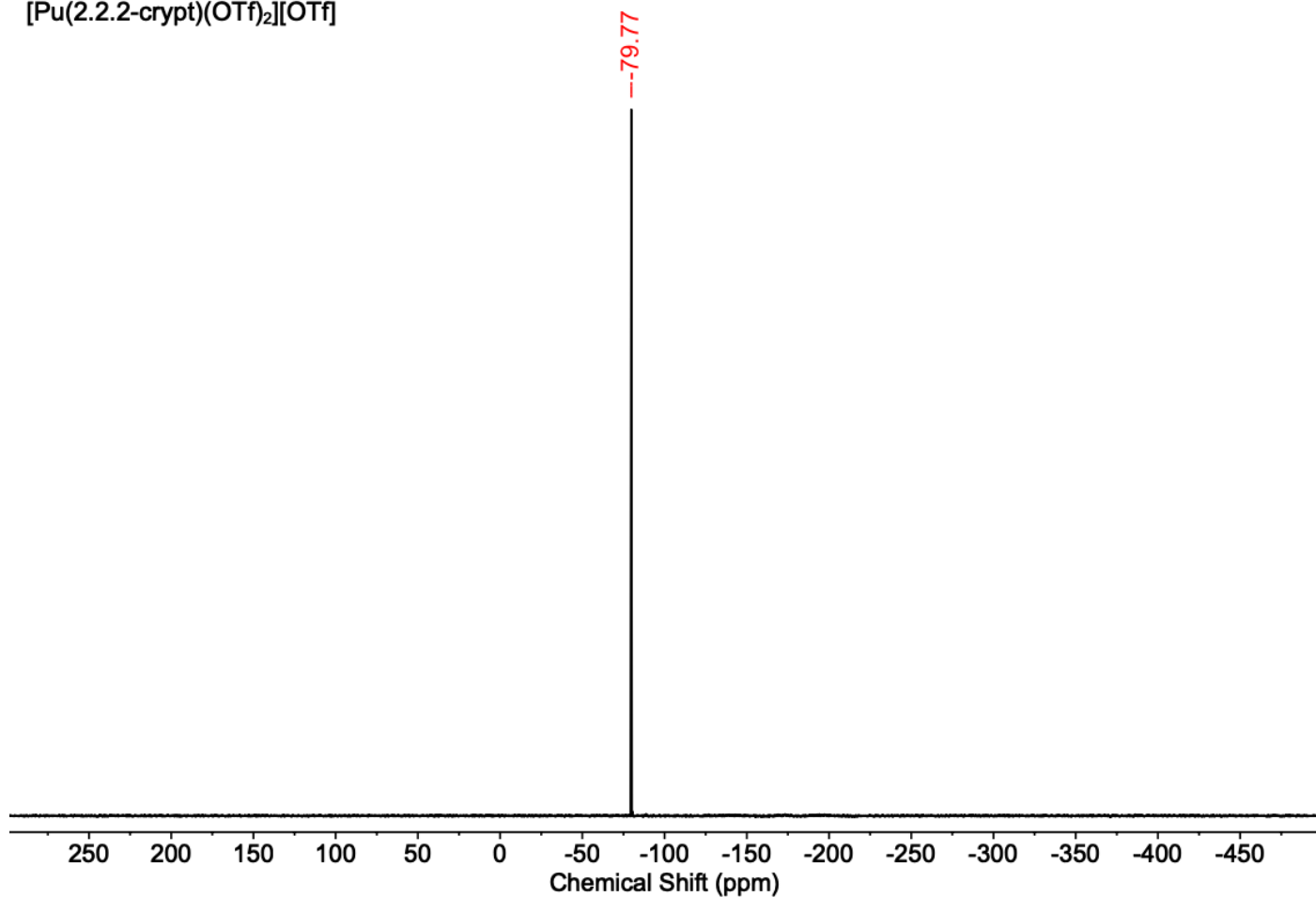
Figure S19. $^{19}F\{^1H\}$ NMR spectrum of [Pu(2.2.2-crypt)(OTf)$_2$][OTf] (**1-Pu**) in THF-d_8 collected at 298 K. No other peaks with significant intensity were observed between ±150 ppm. The presence of a single peak suggests that the bound and outer-sphere OTf ligands are in equilibrium at room temperature. The artefacts between –225 and –150 are due to the FEP NMR tube liner that are part of our radiological control protocol. See below (Figure S20 and Figure S21) for spectra of a blank FEP tube.
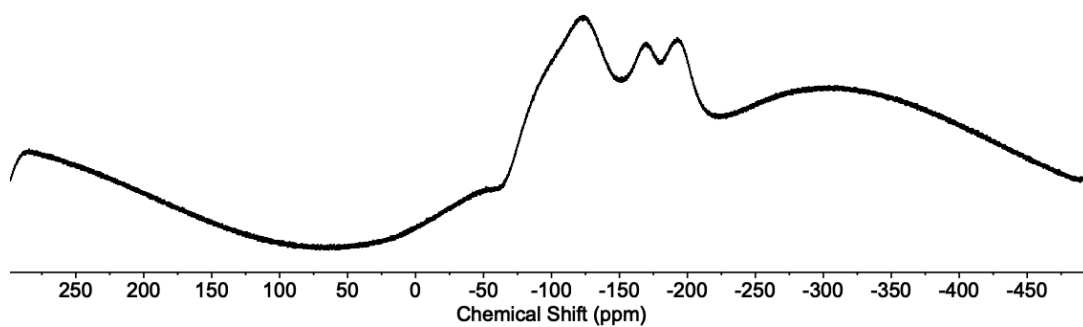
Figure S20. ^{19}F NMR spectrum of a blank FEP NMR tube liner inside a borosilicate NMR tube.

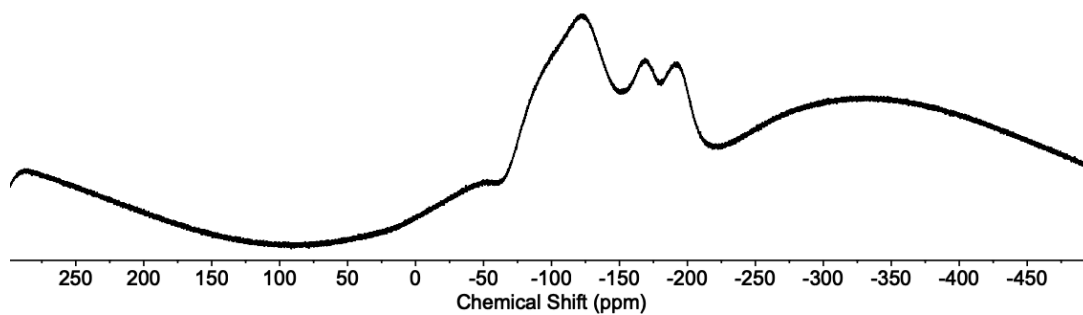**Figure S21.** ^{19}F{^{1}H} NMR spectrum of a blank FEP NMR tube liner inside a borosilicate NMR tube.

S6. Computational Details

Electronic structure calculations on $[An(crypt)OTf_2]^{3+}$ (An = U, Np and Pu) were carried out at the density functional level of theory using the TPSSh[8] functional with Grimme's D3 dispersion correction[14] in C_1 symmetry. Scalar relativistic effective core potentials (ECPs)[15] with the def-SV(P)[16] basis set were used for all metals and polarized split-valence basis sets with diffuse functions def2-SV(P)[17] were used for the lighter atoms. DFT quadrature grids of size 4 were used throughout.[18] The continuum solvation model COSMO[19] with a dielectric constant of 7.520 and a refractive index of 1.3 for THF[20] was included to account for solvent effects. All structures were initially optimized starting from the X-ray structures without symmetry constraints and with geometry convergence thresholds of 10^{-4} a.u and energy convergence of 10^{-7} a.u. Optimized structures were confirmed to be minima on the potential energy surface by vibrational analysis using finite differences of gradients. Vertical excitation energies and oscillator strengths of the solvent optimized structures were carried within the time-dependent density functional theory (TDDFT) framework using def2-SVPD[21] basis sets for the ligands and def-SV(P) basis set for Pu and Np. UV-vis-NIR spectra were simulated using Gaussian line profiles with a root mean-square width of 0.1 eV. Molecular orbitals and electronic transitions and states were analyzed with VMD[22] and Mulliken population analysis (MPA). All calculations were carried out with the TURBOMOLE program suite, Version V-7.5.[23]

$[U(crypt)(OTf)_2]^{1+}$

The solvent optimized structure of $[U(crypt)(OTf)_2]^{1+}$ was found to have C_1 symmetry with $5f^3$ occupation. The structure is in qualitative agreement with the X-ray data with the U-O(OTf) distance being ~8 pm shorter. To understand the $5f$ ligand field splitting, $[U(crypt)]^{3+}$ was modelled without the OTf$^-$ ligands starting from the highest possible symmetry, D_3. Structure optimization of $[U(crypt)]^{3+}$ in D_3 symmetry yielded a saddle point exhibiting a second order Jahn-Teller distortion into C_2 and an additional distortion into C_1. Nevertheless, the D_3-symmetric ligand field splitting is compatible with a non-degenerate ground state, Figure S21. Occupation of 22 a_2 in $[U(crypt)]^{3+}$ with f_z^3 character which transforms to 197 a in $[U(crypt)(OTf)_2]^{1+}$, is energetically unfavorable due to repulsive interactions with the nitrogen lone pairs pointing along the threefold symmetry axis, Figure

1. The degenerate 38 e highest occupied molecular orbitals (HOMO) correspond to the $[f_{xz}^2, f_{yz}^2]$ pair while the lowest unoccupied molecular orbitals (LUMO) are the $[f_{xyz}, f_{z(x^2-y^2)}]$ pair. Figure 1 shows the molecular orbital diagram for the D_3-symmetric and C_1-symmetric ligand field splitting of $[U(crypt)]^{3+}$ and the corresponding C_1-symmetric ligand field splitting of $[U(crypt)(OTf)_2]^{1+}$. The optimized structure of $[U(crypt)]^{3+}$ is in qualitative agreement with the experimental one. However, the theoretically calculated average U-O and U-N bond distances are ~19 pm and ~12 pm shorter than the corresponding experimental values, Table S2. The shortening of these bonds are consistent with a decrease in coordination number of the complex compared to $[U(crypt)(OTf)_2]^{1+}$. The average O-U-O bond angle was 62.66° and the N-U-N bond angle was 163.76°.

Table S2. Relevant metal-ligand distances from the structures optimized in C_1 symmetry for $[U(crypt)]^{3+}$ and $[U(crypt)(OTf)_2]^{1+}$.

Complex	Bonded Atoms	Bond Length (Å)
$[U(crypt)]^{3+}$	U-N	2.69
	U-O1	2.48
	U-O2	2.48
	U-O3	2.50
$[U(crypt)(OTf)_2]^{1+}$	U-N	2.797
	U-O1	2.606
	U-O2	2.632
	U-O3	2.636
	U-OTf	2.406

[U(crypt)]³⁺

7s, 7p Rydberg

22 a₂ f_{z^3}

40 e $d_{x^2-y^3}$, d_{xy}

21 a₂ $f_{y(3x^2-y^2)}$
39 e $[f_{z(x^2-y^2)}, f_{xyz}]$

38 e $[f_{xz^2}, f_{yz^2}]$

23 a₁ $f_{x(x^2-3y^2)}$

D_3

7s, 7p Rydberg

d_{z^2}, d_{xy}

123 a f_{z^3}
122 a f_{xyz}
121 a $f_{y(3x^2-y^2)}$
120 a $f_{z(x^2-y^2)}$

119 a $f_{x(x^2-3y^2)}$
118 a f_{yz^2}
117 a f_{xz^2}

C_1

[U(crypt)OTf₂]³⁺

7s, 7p Rydberg

d_{yz}, $d_{x^2-y^2}$
ligand

197 a f_{z^3}
196 a f_{xyz}
195 a $f_{y(3x^2-y^2)}$
194 a $f_{z(x^2-y^2)}$

193 a f_{yz^2}
192 a $f_{x(x^2-3y^2)}$
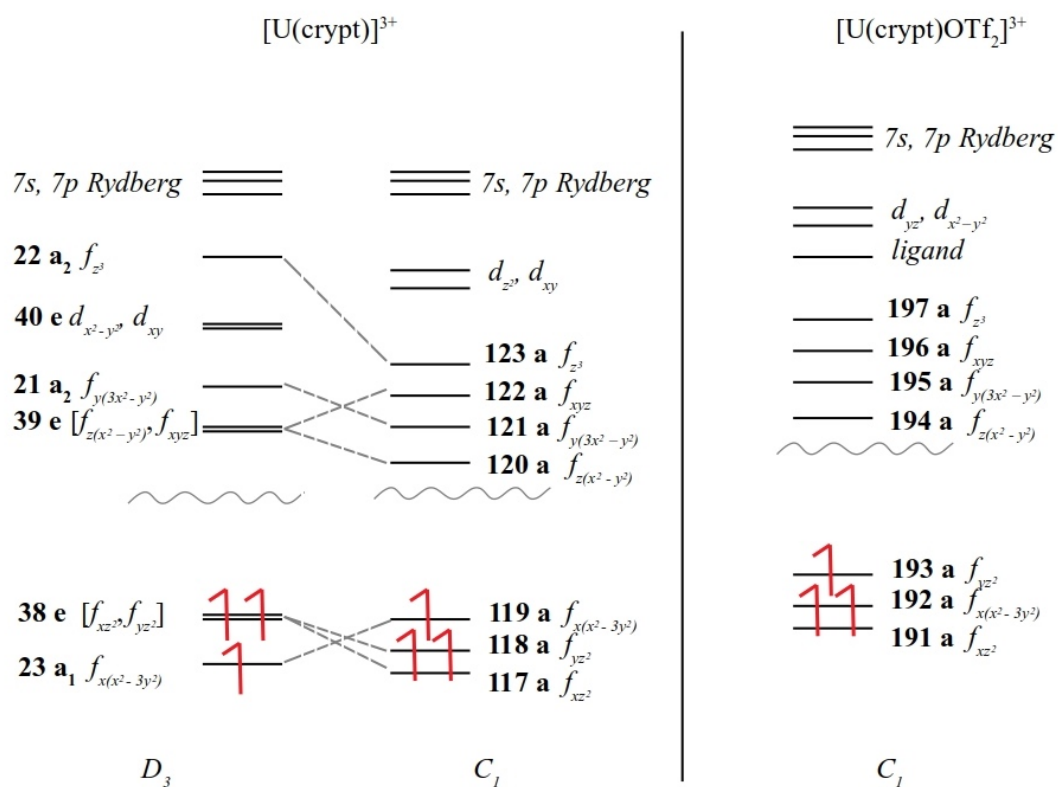**191 a** f_{xz^2}

C_1

Figure S22. Qualitative molecular orbital diagram for the ground state of [U(crypt)]³⁺ and [U(crypt)(OTf)₂]¹⁺ showing the α spin frontier orbitals (not to scale). Other unoccupied orbitals with 6d character are higher in energy and are not displayed here.
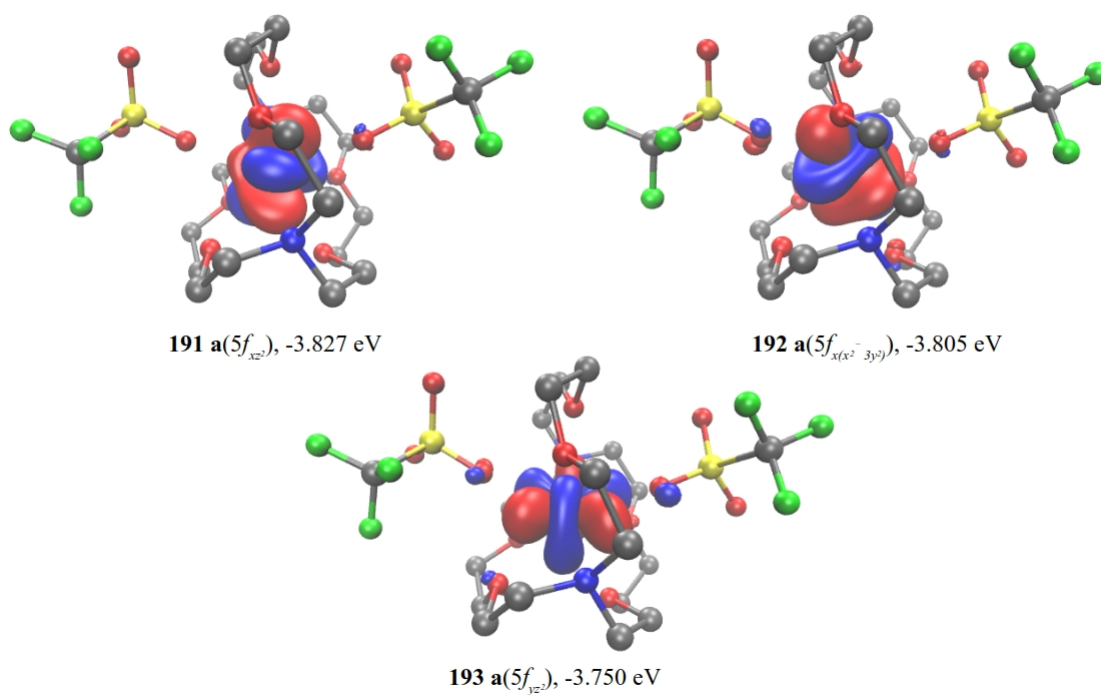
191 a($5f_{xz^2}$), -3.827 eV

192 a($5f_{x(x^2-3y^2)}$), -3.805 eV

193 a($5f_{yz^2}$), -3.750 eV

Figure S23. Highest occupied molecular orbitals of [U(crypt)(OTf)$_2$]$^{1+}$ plotted with contour values of ±0.05

194 a($5f_{z(x^2-y^2)}$), -0.980 eV

195 a($5f_{y(3x^2-y^2)}$), -0.935 eV

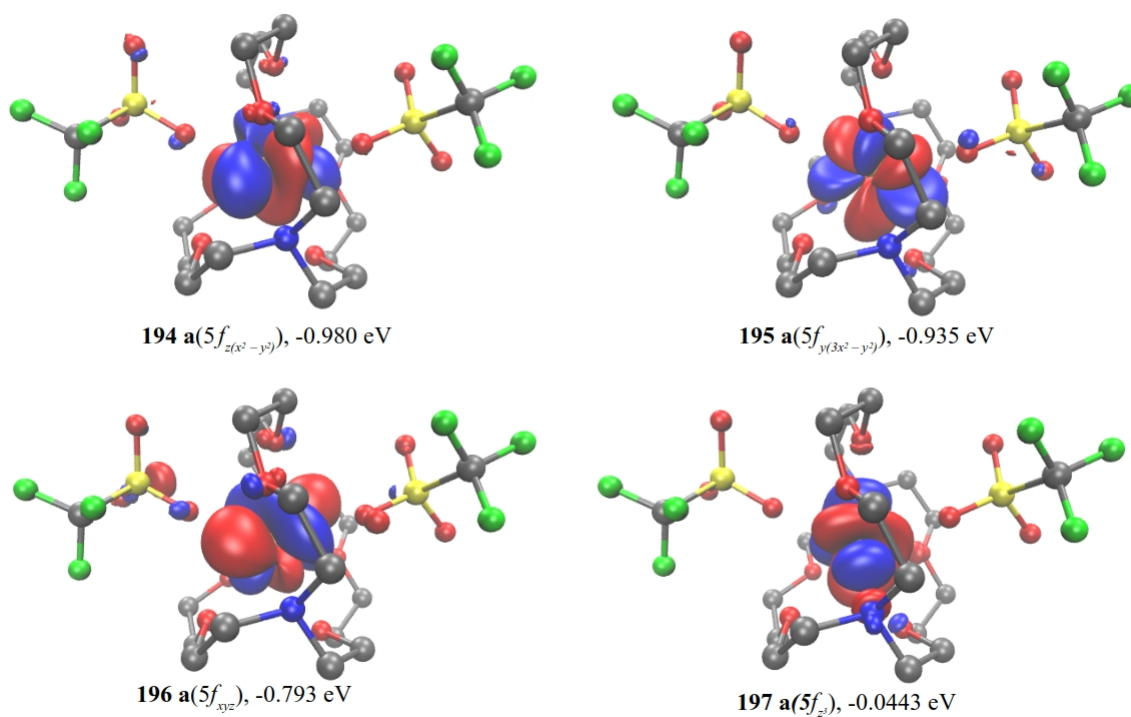**196 a($5f_{xyz}$), -0.793 eV**

197 a($5f_{z^3}$), -0.0443 eV

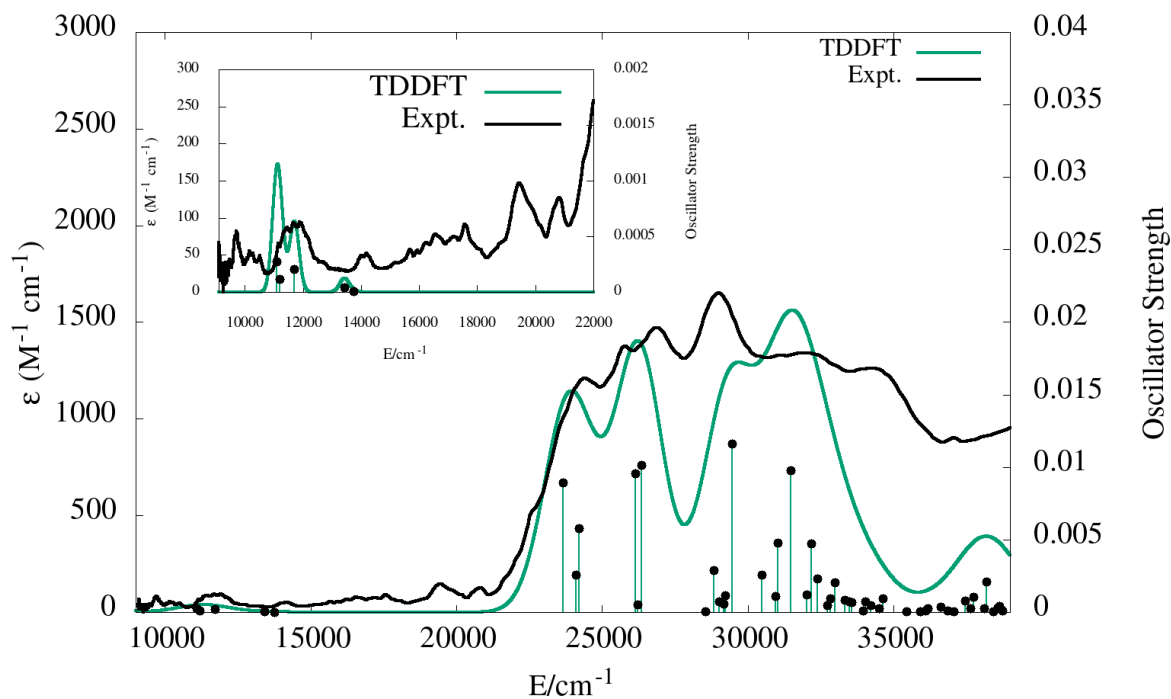**Figure S24.** Lowest unoccupied molecular orbitals of [U(crypt)(OTf)$_2$]$^{1+}$ plotted with contour values of ±0.05

31

Figure S25. Simulated UV-vis-NIR spectrum of [U(crypt)OTf₂]¹⁺ with computed TDDFT oscillator strengths shown as vertical lines. A Gaussian line broadening of 0.10 eV was applied. The computed intensities were scaled by a factor 0.5 to ease comparison with the experimental spectrum [inset: a Gaussian line broadening of 0.02 eV was applied. The computed intensities were scaled by a factor 0.5 to ease comparison with the experimental spectrum].
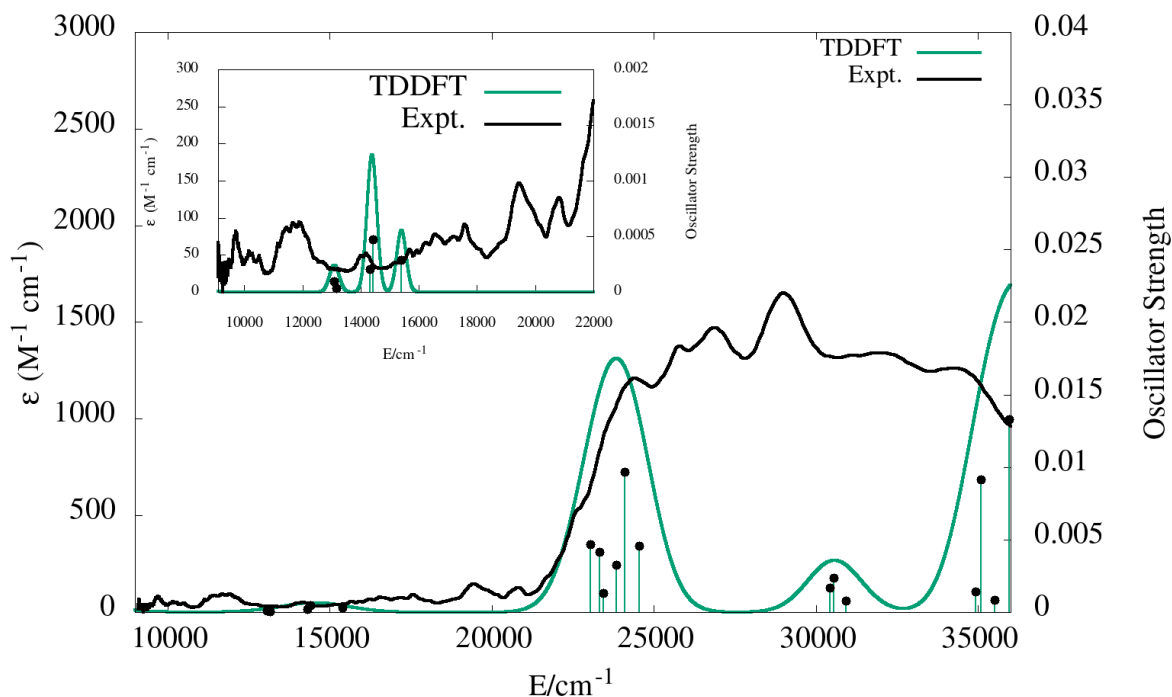
Figure S26. Simulated UV-vis-NIR spectrum of [U(crypt)]³⁺ with computed TDDFT oscillator strengths shown as vertical lines. A Gaussian line broadening of 0.10 eV was applied and the computed excitation energies were empirically blue-shifted by 0.2 eV. The computed intensities were scaled by a factor 0.5 to ease comparison with the experimental spectrum [inset: a Gaussian line broadening of 0.02 eV was applied and the computed excitation energies were empirically blue-shifted by 0.2 eV. The computed intensities were scaled by a factor 0.5 to ease comparison with the experimental spectrum].

The computed excitation spectrum for [U(crypt)(OTf)₂]¹⁺ shows $f{\rightarrow}d$ transitions between 25000-33000 cm⁻¹. The excitations between 7000-20000 cm⁻¹ arise from $f{\rightarrow}f$ transitions with very low oscillator strengths. The presence of the OTf⁻ ligands resulted in significant d-orbital splitting accounting for more $f{\rightarrow}d$ transitions in [U(crypt)(OTf)₂]¹⁺. The [U(crypt)]³⁺ spectrum is artificially red-shifted by ~0.2 eV.

Table S3: Electronic excitation summary for $[U(crypt)(OTf)_2]^{1+}$ computed using the TPSSh functional with the def2-SVPD basis set for ligand atoms. All excitations computed are single excitations involving alpha spin to alpha spin transitions. Oscillator strengths are reported in the length gauge.

Wavelength (cm^{-1})	Oscillator Strength (len)	Dominant Contributions			Assignment
		Occupied	Virtual	% weight	
11206	0.0001	191a	196a	27.0	$5f_{xz}^2 \rightarrow 5f_{xyz}$
		192a	194a	22.6	$5f_{x(x^2-3y^2)} \rightarrow 5f_{z(x^2-y^2)}$
11707	0.0005	193a	196a	33.1	$5f_{yz}^2 \rightarrow 5f_{xyz}$
		191a	194a	23.5	$5f_{xz}^2 \rightarrow 5f_{z(x^2-y^2)}$
24093	0.00414	191a	199a	59.0	$5f_{xz}^2 \rightarrow 6d_{yz}$
		192a	199a	17.1	$5f_{x(x^2-3y^2)} \rightarrow 6d_{yz}$
26220	0.00119	193a	200a	23.9	$5f_{yz}^2 \rightarrow 6d_{x^2-y^2}$
		192a	200a	23.5	$5f_{x(x^2-3y^2)} \rightarrow 6d_{x^2-y^2}$
28547	0.00007	193a	198a	71.8	$5f_{yz}^2 \rightarrow$ ligand
		193a	200a	13.0	$5f_{yz}^2 \rightarrow 6d_{x^2-y^2}$
26355	0.0102	191a	200a	41.1	$5f_{xz}^2 \rightarrow 6d_{x^2-y^2}$
		192a	200a	14.5	$5f_{x(x^2-3y^2)} \rightarrow 6d_{x^2-y^2}$

[Np(crypt)(OTf)$_2$]$^{1+}$

The solvent optimized structure of [Np(crypt)(OTf)$_2$]$^{1+}$ resulted in a C_1 symmetric minimum, a quintet (S = 4) state with $5f^4$ occupation. Similar to [U(crypt)]$^{3+}$ occupation of 22 a$_2$ in [Np(crypt)]$^{3+}$ with mostly f_z^3 character which transform to 197 a in [Np(crypt)(OTf)$_2$]$^{1+}$, is energetically unfavorable due to repulsive interactions with the nitrogen lone pairs pointing along the symmetry axis, Figure S26. The two lowest lying degenerate orbitals 39 e in [Np(crypt)]$^{3+}$ which transform to 195 a and 196 a in [Np(crypt)(OTf)$_2$]$^{1+}$ exhibit significant f character due to minimal splitting in the f manifold. Orbitals 198a and 200a exhibit significant $6d$ character. The optimized structure of [Np(crypt)]$^{3+}$ is in qualitative agreement with the one obtained from X-ray analysis, except for the average Np-O and Np-N distances that are shorter by ~7 and ~13 pm, Table S4. This shortening of bond lengths may be due to the removal of the OTf- ligands as discussed above for the neglect of OTf$^-$ ligands in [U(crypt)]$^{3+}$. The average O-Np-O bond angle was 63.8° and the N-Np-N bond angle was 176.4°.

Table S4. Relevant metal-ligand distances from the structures optimized in C_1 symmetry for [Np(crypt)]$^{3+}$ and [Np(crypt)(OTf)$_2$]$^{1+}$.

Complex	Bonded Atoms	Bond Length (Å)
[Np(crypt)]$^{3+}$	Np-N	2.607
	Np-O1	2.483
	Np-O2	2.496
	Np-O3	2.480
[Np(crypt)(OTf)$_2$]$^{1+}$	Np-N	2.772
	Np-O1	2.616
	Np-O2	2.642
	Np-O3	2.591
	Np-OTf	2.392
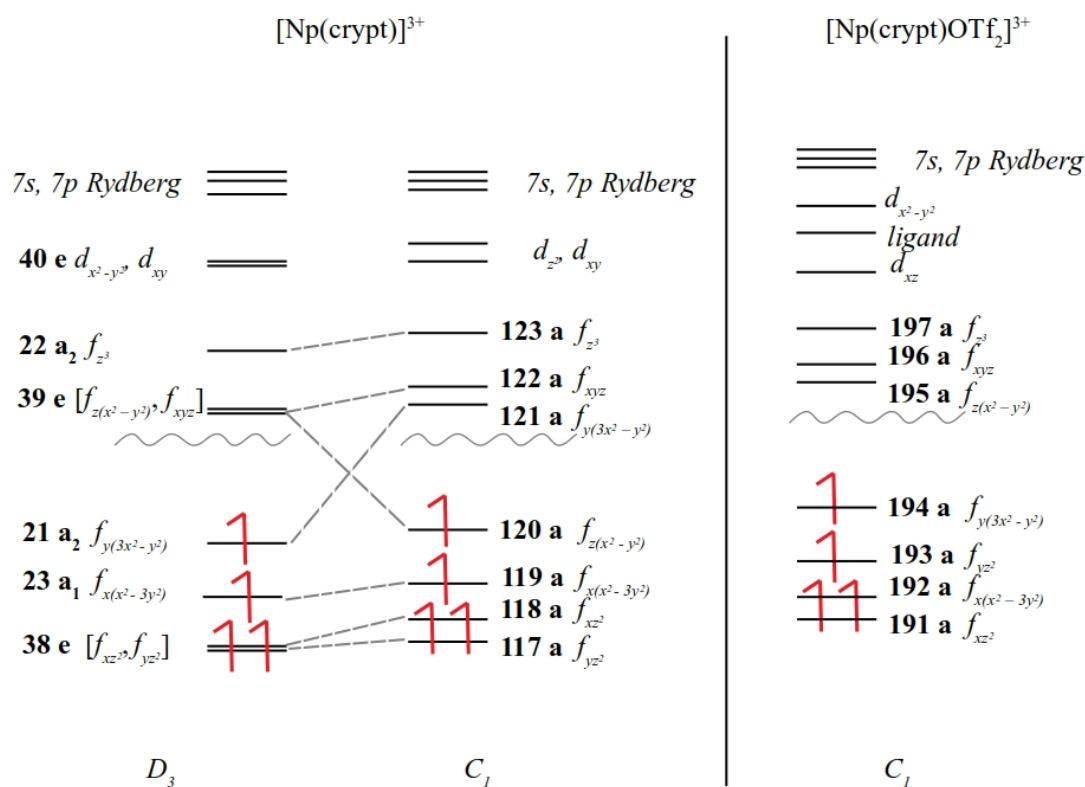
Figure S27. Qualitative molecular orbital diagram for the ground state of [Np(crypt)]³⁺ and [Np(crypt)(OTf)₂]¹⁺ showing the α spin frontier orbitals (not to scale). Other unoccupied orbitals with 6d character are higher in energy and are not displayed here.
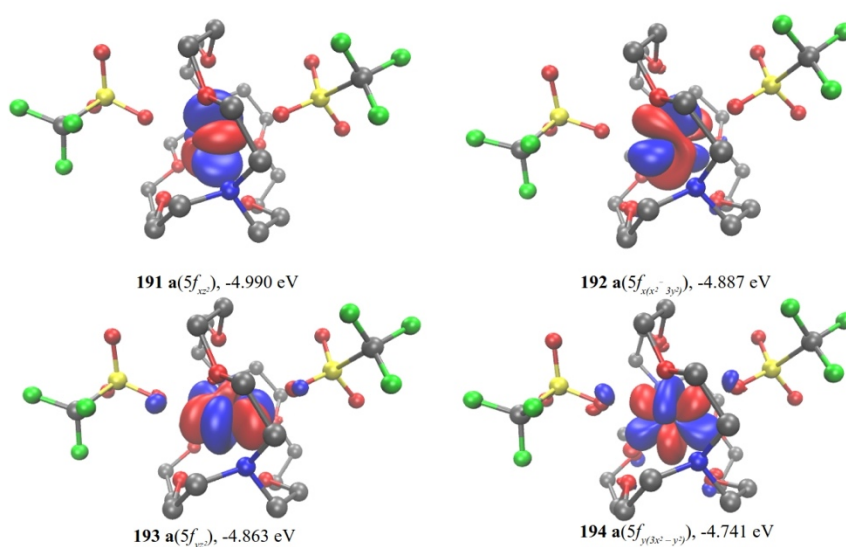

Figure S28. Highest molecular orbitals of [Np(crypt)(OTf)₂]¹⁺ plotted with contour values of ±0.05.

195 a$(5f_{z(x^2-y^2)})$, -1.879 eV

196 a$(5f_{xyz})$, -1.854 eV

197 a$(5f_{z^3})$, -1.659 eV

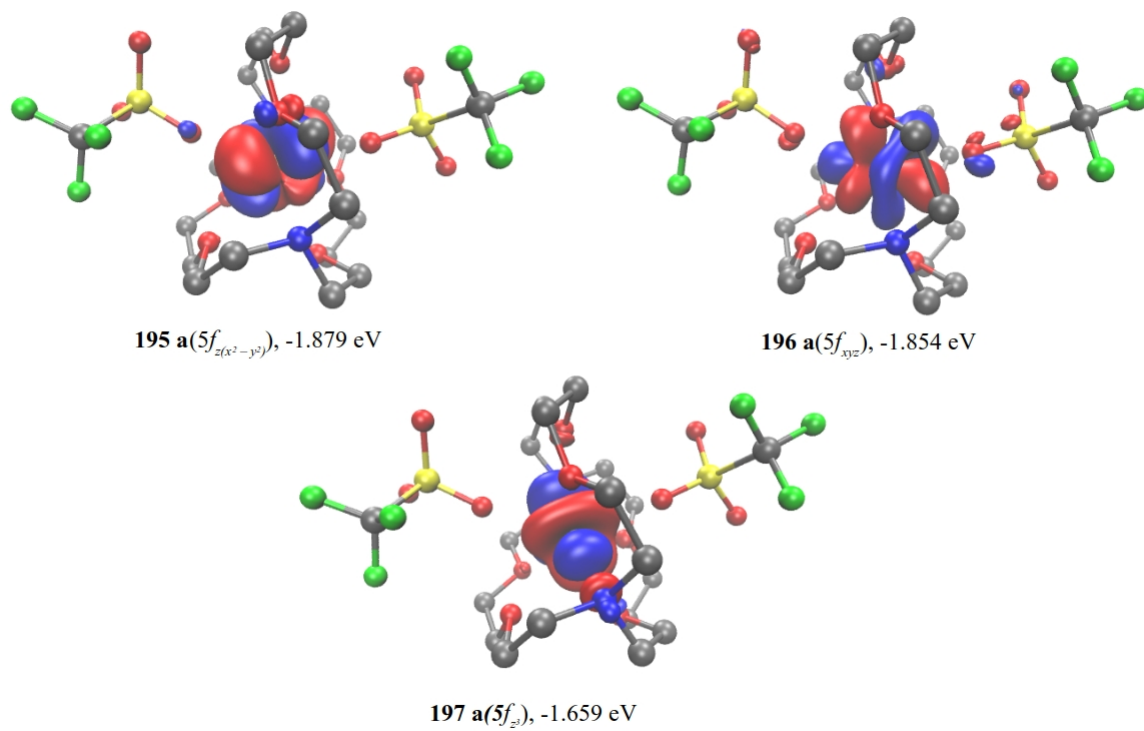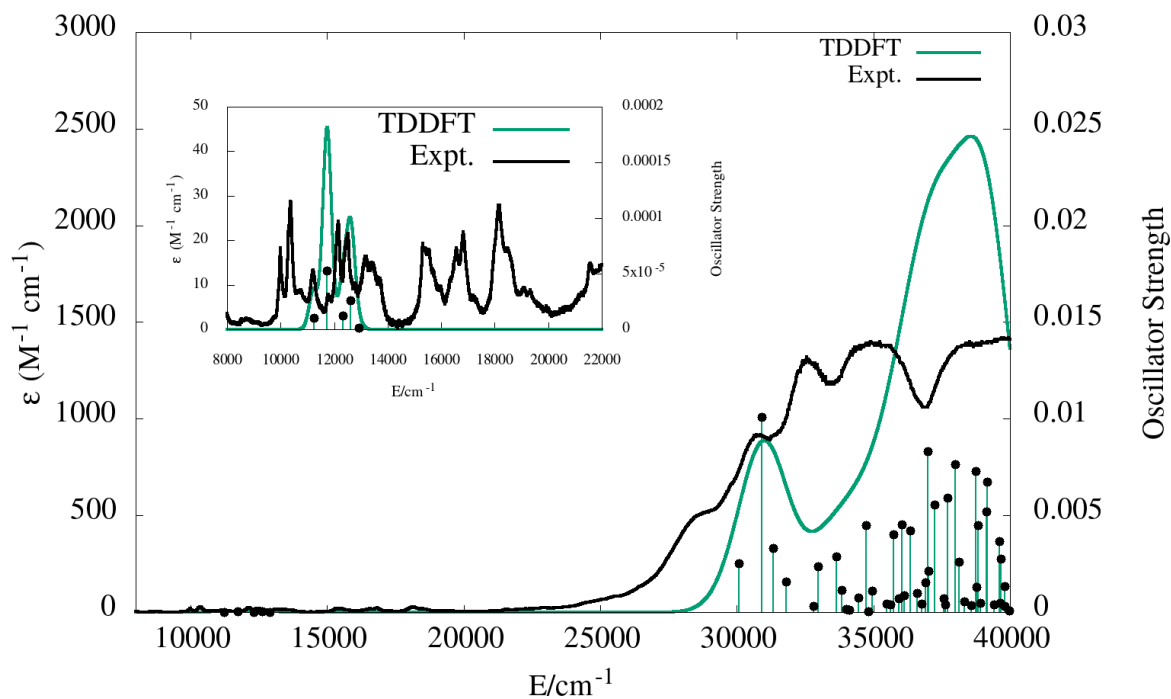**Figure S29.** Lowest unoccupied molecular orbitals of [Np(crypt)(OTf)$_2$]$^{1+}$ plotted with contour values of ±0.05

Figure S30. Simulated UV-vis-NIR spectrum of [Np(crypt)(OTf)$_2$]$^{1+}$ with computed TDDFT oscillator strengths shown as vertical lines. A Gaussian line broadening of 0.10 eV was applied. The computed intensities were scaled by a factor 0.5 to ease comparison with the experimental spectrum [inset: a Gaussian line broadening of 0.02 eV was applied. The computed intensities were scaled by a factor 1.5 to ease comparison with the experimental spectrum].
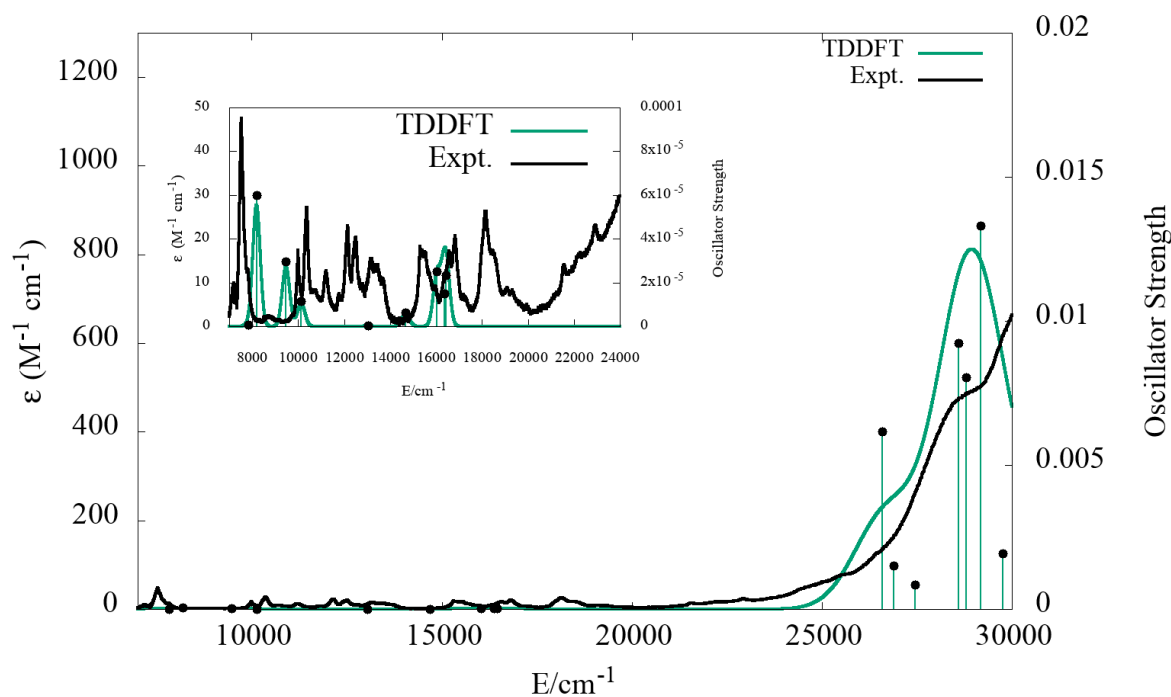
Figure S31. Simulated UV-vis-NIR spectrum of [Np(crypt)]$^{3+}$ with computed TDDFT oscillator strengths shown as vertical lines. A Gaussian line broadening of 0.10 eV was applied and the computed excitation energies were empirically blue-shifted by 0.3 eV. The computed intensities were scaled by a factor 0.1 to ease comparison with the experimental spectrum [inset: a Gaussian line broadening of 0.02 eV was applied and the computed excitation energies were empirically blue-shifted by 0.3 eV. The computed intensities were scaled by a factor 0.5 to ease comparison with the experimental spectrum].

Similar to the spectrum of [U(crypt)(OTf)$_2$]$^{1+}$, the relatively intense *f→d* transitions occur between 25000-33000 cm^{-1} while the relatively low intense *f→f* transitions occur between 7000-20000 cm^{-1}. The [Np(crypt)]$^{3+}$ spectrum was artificially red-shifted by ~0.3 eV.

Table S5: Electronic excitation summary for $[Np(crypt)(OTf)_2]^{1+}$ computed using the TPSSh functional with the def2-SVPD basis set for ligand atoms. All excitations computed are single excitations involving alpha spin to alpha spin transitions. Oscillator strengths are reported in the length gauge.

Wavelength (cm^{-1})	Oscillator Strength (len)	Dominant Contributions			
		Occupied	Virtual	% weight	Assignment
11231	0.00001	192a	196a	36.5	$5f_{x(x^2-3y^2)} \rightarrow 5f_{xyz}$
		194a	195a	29.5	$5f_{y(3x^2-y^2)} \rightarrow 5f_{z(x^2-y^2)}$
		192a	195a	10.8	$5f_{x(x^2-3y^2)} \rightarrow 5f_{z(x^2-y^2)}$
		194a	196a	9.4	$5f_{y(3x^2-y^2)} \rightarrow 5f_{xyz}$
12331	0.00001	194a	197a	40.3	$5f_{y(3x^2-y^2)} \rightarrow 5f_{z^3}$
		191a	196a	25.1	$5f_{xz^2} \rightarrow 5f_{xyz}$
		191a	195a	16.5	$5f_{xz^2} \rightarrow 5f_{z(x^2-y^2)}$
		191a	197a	5.1	$5f_{xz^2} \rightarrow 5f_{z^3}$
12623	0.00002	193a	197a	37.3	$5f_{yz^2} \rightarrow 5f_{z^3}$
		192a	196a	17.8	$5f_{x(x^2-3y^2)} \rightarrow 5f_{xyz}$
		193a	196a	11.4	$5f_{yz^2} \rightarrow 5f_{xyz}$
32820	0.00033	194a	198a	80.7	$5f_{y(3x^2-y^2)} \rightarrow 6d_{xz}$
34008	0.00017	192a	198a	72.8	$5f_{x(x^2-3y^2)} \rightarrow 6d_{xz}$
34732	0.0045	194a	200a	25.0	$5f_{y(3x^2-y^2)} \rightarrow 6d_{x^2-y^2}$
		194a	199a	16.7	$5f_{y(3x^2-y^2)} \rightarrow$ ligand

$[Pu(crypt)(OTf)_2]^{1+}$

The solvent optimized structure of $[Pu(crypt)(OTf)_2]^{1+}$ resulted in a C_1 symmetric minimum, a sextet ($S = 5$) state with $5f^5$ occupation. Similar to $[U(crypt)(OTf)_2]^{3+}$ and $[Np(crypt)(OTf)_2]^{3+}$ 197 a remain unoccupied with mostly f_{z^3} character, Figure S31. The optimized structure is in qualitative agreement with the one obtained from X-ray analysis, except for the average Pu-O and Pu-N distances that are

shorter by ~1 and ~4 pm, Table S6. However the solvent optimized structure predicts the OTf⁻ to be more strongly bound to the metal center, yielding ~10 pm shorter bond lengths.

Table S6. Relevant metal-ligand distances from the structures optimized in C_1 symmetry for $[Pu(crypt)]^{3+}$ and $[Pu(crypt)(OTf)_2]^{1+}$.

Complex	Bonded Atoms	Bond Length (Å)
$[Pu(crypt)]^{3+}$	Pu-N	2.590
	Pu-O1	2.469
	Pu-O2	2.480
	Pu-O3	2.463
$[Pu(crypt)(OTf)_2]^{1+}$	Pu-N	2.747
	Pu-O1	2.607
	Pu-O2	2.638
	Pu-O3	2.600
	Pu-OTf	2.380
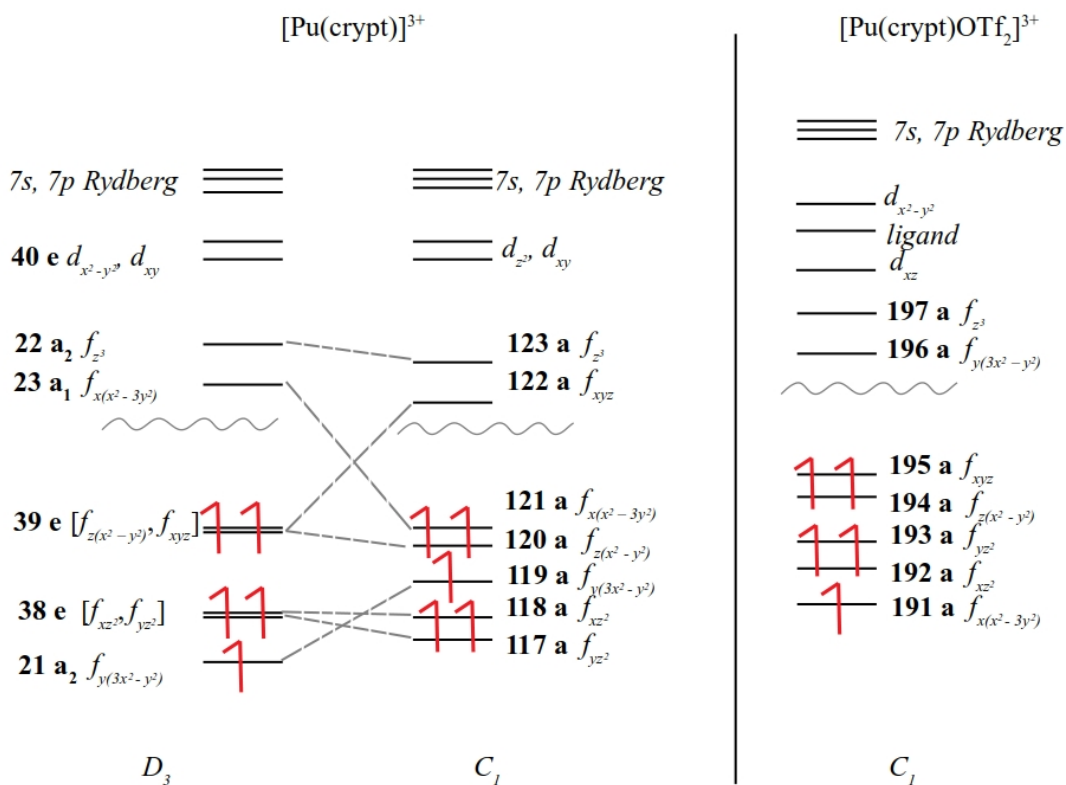
Figure S32. Qualitative molecular orbital diagram for the ground state of [Pu(crypt)]³⁺ and [Pu(crypt)(OTf)₂]¹⁺ showing the α spin frontier orbitals (not to scale). Other unoccupied orbitals with 6d character are higher in energy and are not displayed here.
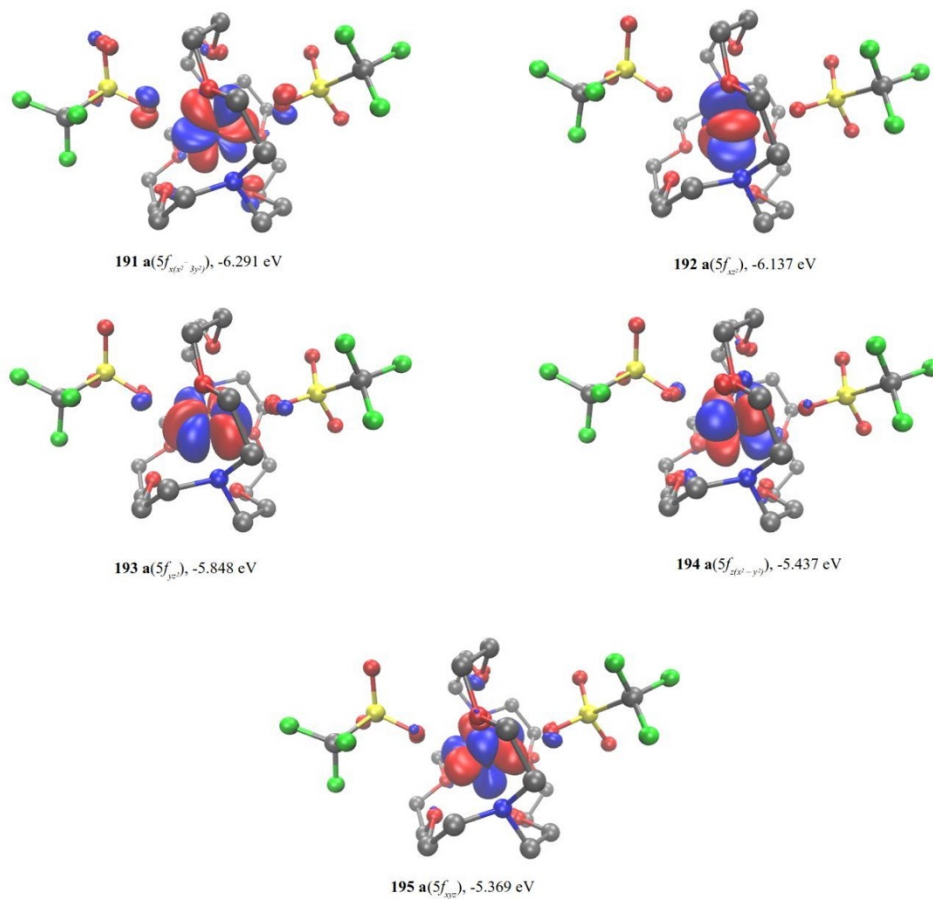
191 a($5f_{x(x^2-3y^2)}$), -6.291 eV

192 a($5f_{xz^2}$), -6.137 eV

193 a($5f_{yz^2}$), -5.848 eV

194 a($5f_{z(x^2-y^2)}$), -5.437 eV

195 a($5f_{xyz}$), -5.369 eV

Figure S33. Highest occupied molecular orbitals of [Pu(crypt)(OTf)$_2$]$^{1+}$ plotted with contour values of ±0.05

196 a($5f_{y(3x^2-y^2)}$), -3.226 eV

197 a($5f_{z^3}$), -2.999 eV

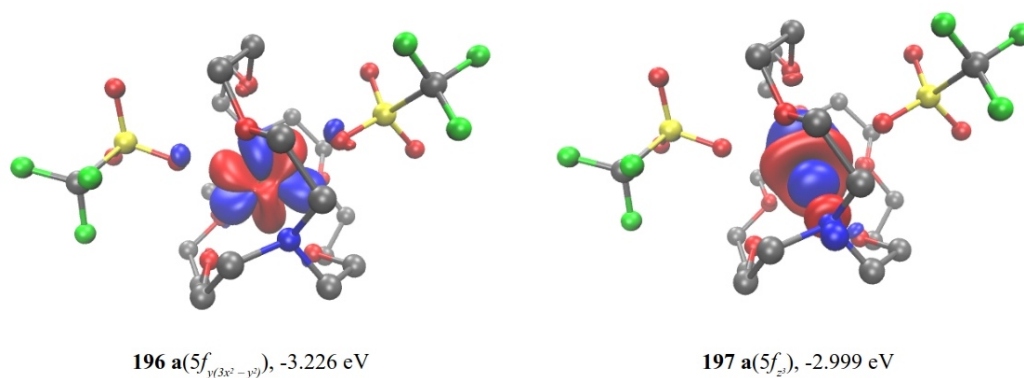**Figure S34.** Lowest unoccupied molecular orbitals of [Pu(crypt)(OTf)$_2$]$^{1+}$ plotted with contour values of ±0.05.

Figure S35. Simulated UV-vis-NIR spectrum of $[Pu(crypt)(OTf)_2]^{1+}$ with computed TDDFT oscillator strengths shown as vertical lines. A Gaussian line broadening of 0.10 eV was applied. The computed intensities were scaled by a factor 0.4 to ease comparison with the experimental spectrum [inset: a Gaussian line broadening of 0.02 eV was applied. The computed intensities were scaled by a factor 1.5 to ease comparison with the experimental spectrum].
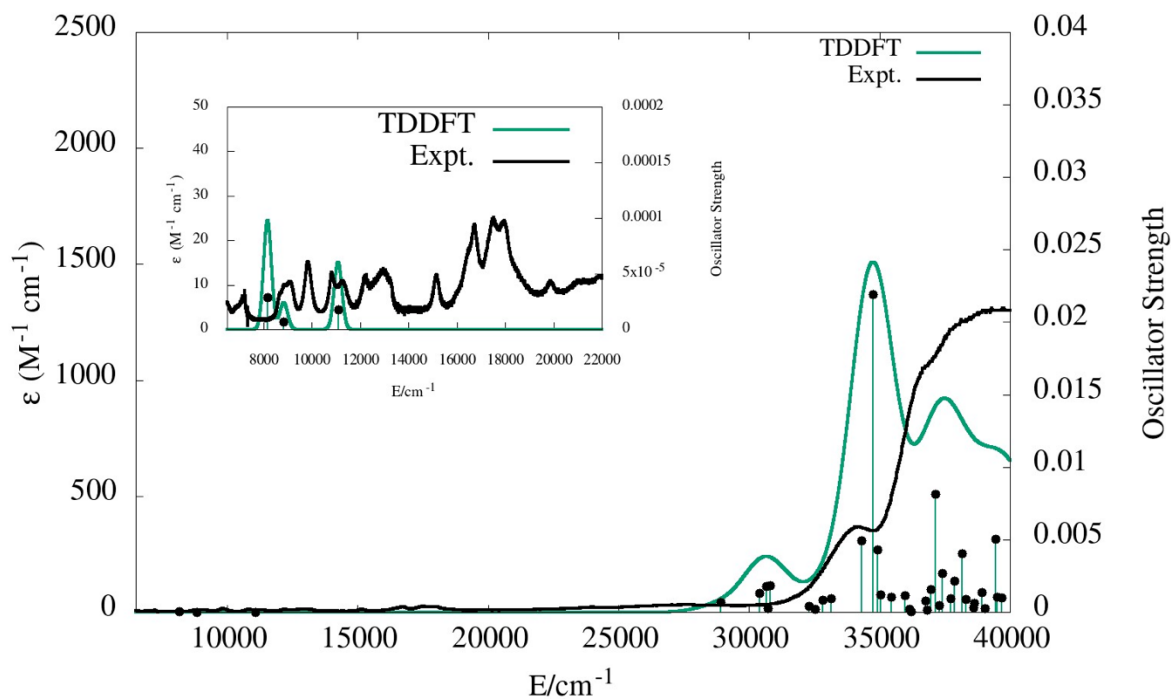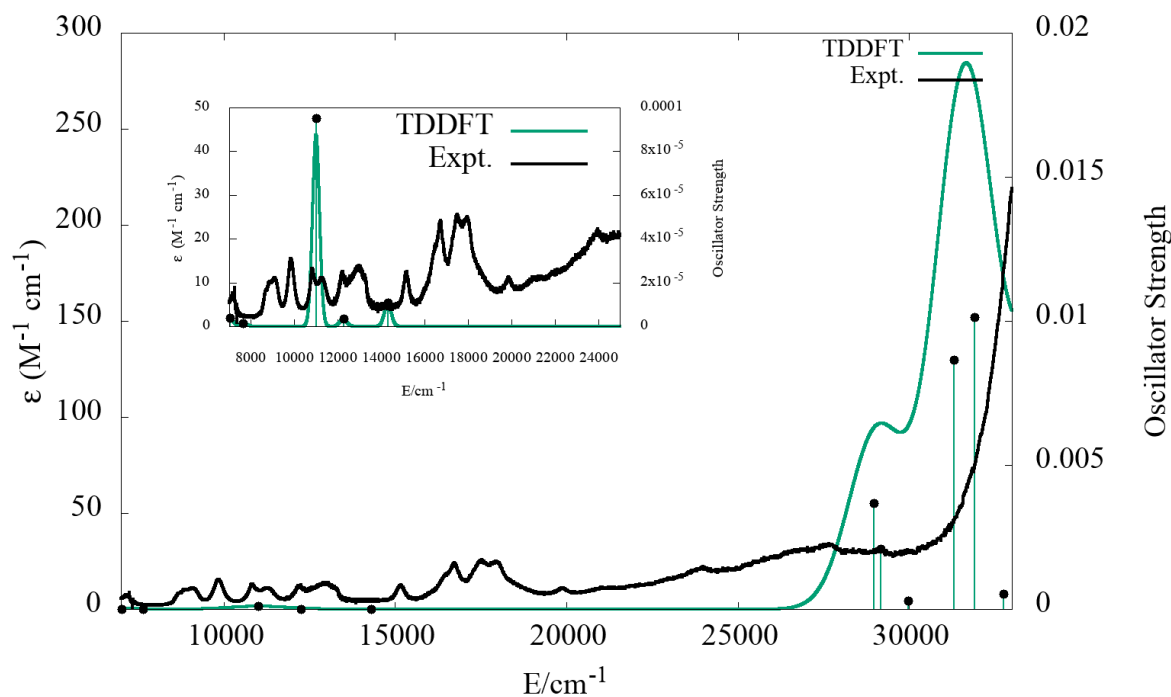
Figure S36. Simulated UV-vis-NIR spectrum of [Pu(crypt)]$^{3+}$ with computed TDDFT oscillator strengths shown as vertical lines. A Gaussian line broadening of 0.10 eV was applied and the computed excitation energies were empirically blue-shifted by 0.2 eV. The computed intensities were scaled by a factor 0.061 to ease comparison with the experimental spectrum [inset: a Gaussian line broadening of 0.02 eV was applied and the computed excitation energies were empirically blue-shifted by 0.2 eV. The computed intensities were scaled by a factor 0.3 to ease comparison with the experimental spectrum].

The computed excitation spectrum for $[Pu(crypt)(OTf)_2]^{1+}$ shows $f{\rightarrow}d$ transitions between 25000-33000 cm^{-1}. The excitations between 7000-20000 cm^{-1} arise from $f{\rightarrow}f$ transitions with very low oscillator strengths. The $[Pu(crypt)]^{3+}$ spectrum was artificially red-shifted by ~0.3 eV.

Table S7: Electronic excitation summary for $[Pu(crypt)(OTf)_2]^{1+}$ computed using the TPSSh functional with the def2-SVPD basis set for ligand atoms. All excitations computed are single excitations involving alpha spin to alpha spin transitions. Oscillator strengths are reported in the length gauge.

Wavelength (cm^{-1})	Oscillator Strength (len)	Dominant Contributions			
		Occupied	Virtual	% weight	Assignment
8172	0.00003	193a	196a	42.5	$5f_{yz^2}{\rightarrow}5f_{y(3x^2-y^2)}$
		194a	197a	28.8	$5f_{z(x^2-y^2)}{\rightarrow}5f_{z^3}$
8844	0.000007	192a	196a	74.4	$5f_{xz^2}{\rightarrow} 5f_{y(3x^2-y^2)}$
		195a	197a	11.3	$5f_{xyz}{\rightarrow} 5f_{z^3}$
11089	0.00002	191a	197a	89.7	$5f_{x(x^2-3y^2)}{\rightarrow}5f_{z^3}$
34308	0.00491	195a	200a	68.2	$5f_{xyz}{\rightarrow} 6d_{x^2-y^2}$
34928	0.0043	194a	200a	61.4	$5f_{z(x^2-y^2)}{\rightarrow}6d_{x^2-y^2}$
36831	0.00015	194a	198a	64.4	$5f_{y(3x^2-y^2)}{\rightarrow} 6d_{xz}$

S7. References

1. NuDat 2.8, Chart of the Nuclides, https://www.nndc.bnl.gov/nudat2/, (accessed 2021-03-05).

2. C. A. P. Goodwin, A. J. Gaunt, M. T. Janicke and B. L. Scott, *J. Am. Chem. Soc.*, 2021, DOI: https://doi.org/10.1021/jacs.1c07967.

3. B. L. Scott, *Actinide Research Quarterly*, Report LA-UR-15-24862, Los Alamos National Laboratory, 2015.

4. APEX2 Version 2014.11-0, Bruker AXS Inc.; Madison, WI, **2014**.

5. SAINT Version 8.34a, Bruker AXS, Inc.; Madison, WI, **2013**.

6. SADABS, Version 2014/5, Bruker AXS, Inc.; Madison, WI.

7. SHELXTL, Version 2014/7, Bruker AXS, Inc.; Madison, WI.

8. V. N. Staroverov, G. E. Scuseria, J. Tao and J. P. Perdew, *J. Chem. Phys.*, 2003, **119**, 12129-12137.

9. CrysAlisPro 39.27b, Oxford Diffraction / Agilent Technologies UK Ltd., Yarnton, U.K.

10. O. V. Dolomanov, L. J. Bourhis, R. J. Gildea, J. A. K. Howard and H. Puschmann, *J. Appl. Crystallogr.*, 2009, **42**, 339-341.

11. (a) G. M. Sheldrick, *Acta Crystallogr. C*, 2015, **71**, 3-8; (b) G. M. Sheldrick, *Acta Crystallogr. A*, 2008, **64**, 112-122.

12. Inkscape: Open Source Scalable Vector Graphics Editor. https://inkscape.org/.

13. W. Clegg, A. J. Blake, J. M. Cole, J. S. O. Evans, P. Main, S. Parsons and D. J. Watkin, *Crystal Structure Analysis*, 2009.

14. (a) S. Grimme, *J. Comput. Chem.*, 2006, **27**, 1787-1799; (b) S. Grimme, J. Antony, S. Ehrlich and H. Krieg, *J. Chem. Phys.*, 2010, **132**, 154104.

15. W. Küchle, M. Dolg, H. Stoll and H. Preuss, *J. Chem. Phys.*, 1994, **100**, 7535-7542.

16. F. Weigend and R. Ahlrichs, *Phys. Chem. Chem. Phys.*, 2005, **7**, 3297-3305.

17. A. Schäfer, H. Horn and R. Ahlrichs, *J. Chem. Phys.*, 1992, **97**, 2571-2577.

18. O. Treutler and R. Ahlrichs, *J. Chem. Phys.*, 1995, **102**, 346-354.

19. A. Klamt and G. Schüürmann, *J. Chem. Soc., Perkin Trans. 2*, 1993, 799-805.

20.   *CRC Handbook of Chemistry and Physics*, CRC Press, Boca Raton, FL., 81st edn., 2008.

21.   D. Rappoport and F. Furche, *J. Chem. Phys.*, 2010, **133**, 134105.

22.   VMD 1.9. http://www.ks.uiuc.edu/Research/vmd/.

23.   TURBOMOLE V7.5 2020, a development of University of Karlsruhe and

       Forschungszentrum Karlsruhe GmbH, 1989-2007, TURBOMOLE GmbH, since 2007;

       available from https://www.turbomole.org.